

Numerical simulation of diurnal and annual performance of coupled solar chimney with earth-to-air heat exchanger system

Tianhe Long^a, Ningjing Zhao^a, Wuyan Li^b, Shen Wei^c, Yongcai Li^{a,*}, Jun Lu^a, Sheng Huang^a, Zhenyong Qiao^a

^aSchool of Civil Engineering, Chongqing University, Chongqing, 400045, China

^bDepartment of Building Science, School of Architecture, Tsinghua University, Beijing, 100084, China

^cThe Bartlett School of Sustainable Construction, University College London (UCL), 1-19 Torrington Place, London, WC1E 7HB, United Kingdom

*Corresponding authors. Tel.: +86 2365123777; E-mail: yongcai85@163.com (Y. Li)

Abstract

The coupled solar chimney with earth-to-air heat exchanger system can passively regulate indoor air quality and thermal environment without electricity cost and carbon emissions. One dynamic model has been established and validated for the system, and using the model this system's diurnal and annual performances were investigated. The simulation results suggested that pipe diameter and length were more critical parameters affecting the system's airflow rate and indoor thermal environment, compared to chimney height and solar collector length. In summer, the airflow rate was significantly different between daytime (260 m³/h) and night-time (50 m³/h). In other seasons, the airflow rate during the daytime increased to around 280 m³/h, and the one during the night-time exceeded 100 m³/h. This system could provide an acceptable airflow rate during daytime, even when solar radiation intensity was low. By the thermal inertia of the subsoil, the annual fluctuation of the air temperature at buried pipe outlet was reduced within 12.8–26.5 °C. The indoor temperature was maintained by the system within the thermal comfort range for most time, with a decreased average indoor air temperature by 4.4 °C in summer and an increased one by 6.4 °C in winter.

Keywords: solar chimney; earth-to-air heat exchanger; diurnal and annual performance; dynamic simulation.

Nomenclature

<i>A</i>	area [m ²]
<i>b</i>	a constant in fitting
<i>a</i>	thermal diffusivity, [m ² /s]
<i>c</i>	specific heat [J/(kg·K)]
<i>D</i>	diameter or equivalent diameter [m]
<i>Fo</i>	Fourier number—dimensionless time
<i>H</i>	height [m]
ΔH	height difference between system inlet and outlet [m]

h_c	convective heat transfer coefficient [W/(m ² ·K)]
h_r	radiant heat transfer coefficient [W/(m ² ·K)]
L	length of flow channel [m]
m_f	mass flow rate of flowing air [kg/s]
m_{f1}	mass flow rate of flowing air per unit area [kg/(m ² ·s)]
Nu	Nusselt number
ΔP	pressure difference [Pa]
Pr	Prandtl number
q	heat flux [W/m ² or W/m]
Re	Reynolds number
R_θ	ratio of two excess temperature solutions
R	radius [m]
T	temperature [K]
$\overline{T_{e,0}}$	annual average temperature at ground surface [K]
U	overall heat transfer coefficient [W/(m ² ·K)]
v	velocity [m/s]
Greeks	
α	absorptivity
β	transmissivity
γ	mean temperature approximation constant
ω	frequency of the yearly variation of ground surface temperature [1/h]
θ	excess temperature [K]
λ	thermal conductivity [W/(m·K)]
ρ	density [kg/m ³]
φ	amplitude of the temperature fluctuation at ground surface [K]
τ	time [s]
δ	thickness [m]
σ	Stefan-Boltzmann constant [5.67×10 ⁻⁸ W/(m ² ·K ⁴)]
ε	emissivity
μ	absolute viscosity [Pa·s]
ξ	minor loss coefficient
ξ_f	friction loss coefficient
Subscripts	
am	ambient
$am - g$	between ambient and glass cover
$am - ins$	between ambient and insulation layer
c	vertical chimney
E	EAHE pipe
$E - f$	between EAHE pipe and flowing air
e	soil
f	flowing air
$f - g$	between flowing air and glass cover

g	glass cover
I	solar irradiation
in	inlet
ins	insulation layer
out	outlet
s	solar collector
sky	sky
$sky - g$	between sky and glass cover
t	total
w	absorber plate
$w - f$	between absorber plate and flowing air
$w - g$	between absorber plate and glass cover

1. Introduction

Buildings are responsible for approximately 40% of global energy use, leading to severe greenhouse gas emissions [1, 2]. Because of the increasing standards of people's life, affordability of air conditioning, universalization of modern architecture, and temperature increase in urban environment, the energy required by the building sector is still expected to increase in the near future [3]. Developing buildings with high energy efficiency has become a priority for sustainable development. One major solution is to develop passive techniques using natural energy [4]. For the air-conditioning of buildings, solar and geothermal energy have captured great attention of researchers [5, 6], and solar chimney (SC) and earth-to-air heat exchanger (EAHE) are two representative techniques for adopting solar energy and geothermal energy, respectively [7, 8].

An SC works mainly based on natural ventilation driven by buoyancy force [9, 10]. It typically contains a glazing cover and an absorber wall to capture the solar radiation, in addition to either an inclined or a vertical air channel with two openings located at the top and bottom, respectively [10, 11]. To increase its ventilation rate and stability, extensive studies have been conducted using numerical or/and experimental approaches to examine the impacts of various factors on its ventilation performance. The inclination angle of an SC is an important consideration. Existing studies suggested that a 45°-inclined SC draws a higher airflow rate than that with other angles [12-15]. Compared to a vertical one, the airflow rate induced by an SC with an inclination angle of 45° is approximately 45% higher under identical conditions [15], due to the reduction in the pressure loss caused by the inclination [16]. Increasing the height of an SC is also beneficial for its ventilation performance, as it increases the solar heat gain and buoyant pressure [17, 18]. Gan [19] suggested that the solar heat gain could be increased by three quarters when increasing the height of an SC by one quarter. Therefore, Du et al. [18] suggested adopting vertical length as long as possible to achieve the best performance, if the length complied with relevant standards. The heat flux of an SC is another significant factor which uses solar radiation to drive the air movement inside the SC. It is well known that a high heat flux can enhance the ventilation rate of an SC.

Manca et al. [20] pointed out that the absorber temperature and airflow rate of an SC were significantly affected by solar radiation. The ventilation rate increases by approximately 30% when solar radiation increases from 300 to 600 W/m². For an SC with a surface area of 2.25 m², the airflow rate increases from 100 m³/h to 350 m³/h when solar radiation rises from 100 W/m² to 1000 W/m² [21]. A higher solar thermal efficiency increases the heat flux for an SC under the same solar irradiance. Absorber plates with high absorptivity and thermal insulation with sufficient thickness are recommended for an SC to enhance its solar thermal efficiency [17, 22].

Fresh air is powered into the pipe of an EAHE generally by mechanical force, and it exchanges heat with the subsoil. Subsequently, the cooled or heated air is sent to an indoor area to improve thermal environment [23, 24]. The heat exchange process and important influencing parameters of an EAHE have been extensively studied. The depth of pipes is an important factor, as a deeply buried pipe implies a small fluctuation amplitude of the surrounding soil temperature. It has been suggested that the buried depth of pipes should be between 1.5 m and 3.5 m not to affect the temperature of the earth by thermal inertia [25, 26]. The diameter and length of pipes are two other important factors, as they determine heat transfer area [27, 28]. The material of the pipe of an EAHE is also a significant consideration. Bojic et al. [29] compared the performance of EAHEs with polyvinyl chloride (PVC) and steel pipes, respectively. Their research results showed that an EAHE with a PVC pipe has the same performance as a steel pipe with the same dimensions. Thus pipe material has little effect on the heat transfer rate of an EAHE. Nevertheless, PVC pipe is recommended as it is cost-effective and anticorrosive.

Both SC and EAHE, however, have drawbacks. For the SC, it is typically used when outdoor air conditions are temperate. Nevertheless, it is no longer desirable when ambient air temperature significantly deviates from thermal comfort limits in hot summer and cold winter, as its cooling potential is low [30]. For the EAHE, a fan is typically used to drive the fresh air from outdoors to indoors through it [31]. Nevertheless, fan operation is accompanied by electricity cost and mechanical noise, leading to higher energy consumption and lower occupant discomfort. Therefore, a coupled SC and EAHE (SCEAHE) system was suggested to avoid the drawbacks [32]. In such a system, fans are not necessary components. Instead, an SC drives fresh air to flow through an EAEH pipe to indoor space. In addition, the cooling and heating capacities provided by the buried pipes extend the operation time of the SC.

Subsequently, a few researchers investigated the coupled SCEAHE system. Li and Yu et al. [33, 34] conducted an experimental study on the feasibility of an SCEAHE system. In their study, the indoor thermal environments were effectively regulated. The indoor air temperature was maintained within 21.3–25.1 °C during the test period. Li et al. [35] conducted a full-scale experiment to investigate the summer system performance of an SCEAHE system. The results showed that the SCEAHE system could successfully induce round-the-clock passive ventilation. The daytime airflow rate can reach up to 253 m³/h due to sufficient solar radiation, whereas a lower nocturnal airflow rate of around 60 m³/h was maintained due to the heat stored in building envelop. Long et al. [36] developed a steady-state model for an SCEAHE to explore how different factors

impact its operating performance.

The previous studies suggest that, as a passive system, the coupled SCEAHE system can regulate both indoor air quality and thermal environment without electricity cost and carbon emissions. Nevertheless, studies concerning the proposed system are quite few. The operating performances of the SCEAHE system during summer and transition seasons were investigated by Li [35] and Long [37] by full-scale experiments, respectively. As experimental approach is time-consuming and expensive, and weather conditions are changeable, their consecutive testing time is not long (seven days). Therefore, the proposed system's long-term, even year-round natural ventilation characteristics need to be studied using numerical methods. The novelty of this work is to develop a comprehensively dynamic model of an SCEAHE system, which involves the coupling of multiple sub-models including solar chimney, EAHE, building, and subsoil. The developed model is run under varying boundary conditions including fluctuating ambient air temperature, solar irradiance, and soil temperature. Furthermore, the diurnal and annual natural ventilation characteristics of the SCEAHE system are investigated. In addition, the evolution of buoyancy force in an annual cycle is also examined. The research findings reinforce the existing literature by means of numerical simulation work and thus contribute to a comprehensive knowledge in the relevant field. The article projective is to reveal the diurnal and annual system operation characteristics of SCEAHE using a validated dynamic model. A parametric study concerning critical components dimensions was first conducted on the system under a summer daily cycle. Moreover, the yearly impacts of the proposed system on the fresh airflow rate, indoor thermal environment, and soil temperature were examined in depth in this study.

2. Modeling of SCEAHE

2.1. Operation mechanism

A schematic of an SCEAHE system was illustrated in Fig. 1. As shown, the solar collector on the roof absorbs solar heat, raises the channel air temperature, and decreases the air density. Buoyant pressure is accordingly generated from the air density difference, and strengthened by the high chimney outlet. The ambient air is driven by the generated buoyancy, sucked into the EAHE pipe, and finally extracted from the chimney outlet. The flowing air exchanges heat with the subsoil. Hence the outlet air temperature is confined within a stable and comfortable range for the room by the relatively constant soil temperature and its thermal inertia. The heat released from the thermal mass and/or the subsoil will maintain the buoyancy force and the airflow rate in the absence of solar radiation.

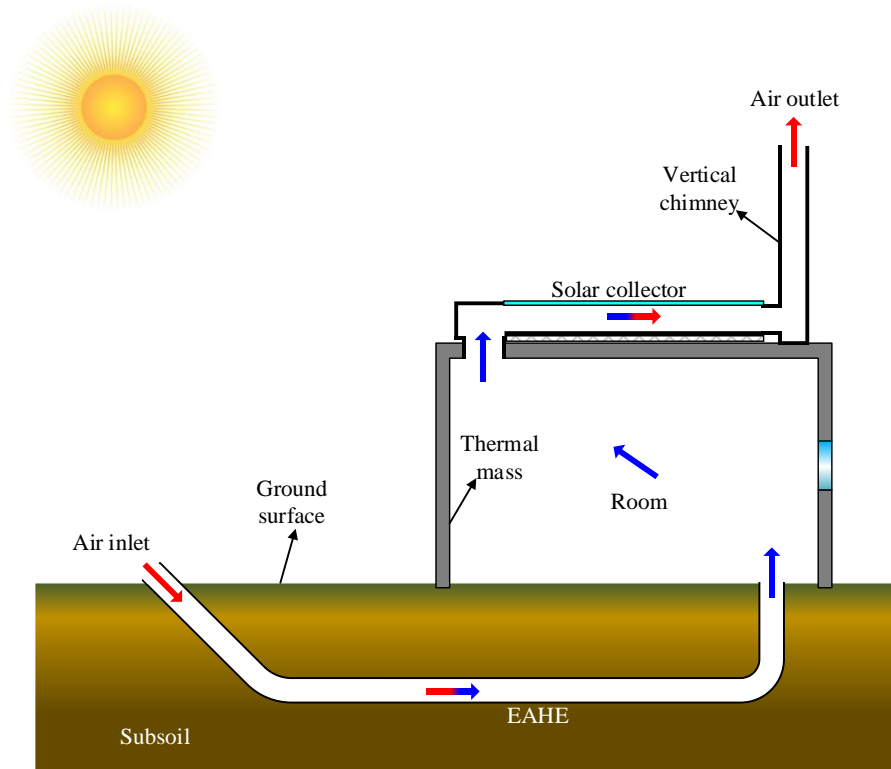


Fig. 1. Schematic of SCEAHE system

2.2. Sub-models of SCEAHE

All the sub-models used in the dynamic model of SCEAHE were presented in this section, excluding the room heat gain model. The room heat gain model can refer to TRNSYS manual 5.4. The pre-set assumptions, governing equations, formulas, and some derivation processes used herein were elaborated in detail, with all equation symbols clearly defined in the nomenclature.

2.2.1. Solar collector

Fig. 2 shows the composition of the solar collector. The assumptions made to simplify the simulation process were listed as follows.

- (1) It is an incompressible flow within the solar collector.
- (2) Heat is only vertically transferred, and horizontal thermal inhomogeneity is not considered.
- (3) The transmissivity of the flowing air equals 1.
- (4) Parameters including temperature, specific heat, and density are lumped for the glass and absorber.

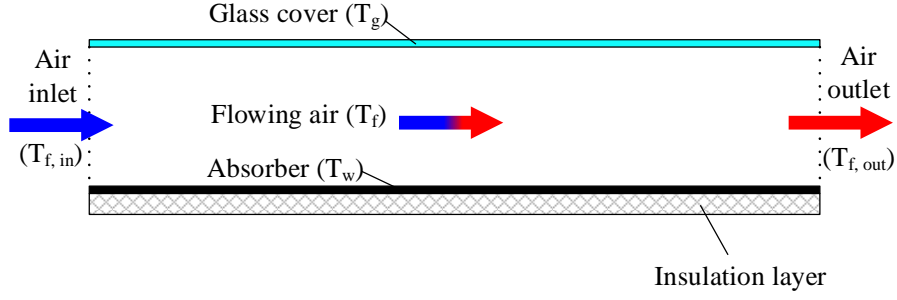


Fig. 2. Physical model of solar collector

Three unsteady-state governing equations were first applied to the solar collector.

For glass cover (T_g):

$$\rho_g c_g \delta_g \frac{dT_g}{dt} = \alpha_g q_I + h_{r,w-g}(T_w - T_g) + h_{c,f-g}(T_f - T_g) + U_g(T_{am} - T_g). \quad (1)$$

For channel air (T_f):

$$\rho_f c_f H_s \frac{dT_f}{dt} = h_{c,w-f}(T_w - T_f) + h_{c,f-g}(T_g - T_f) + m_{f1} c_f (T_{f,in} - T_{f,out}). \quad (2)$$

For absorber plate (T_w):

$$\rho_w c_w \delta_w \frac{dT_w}{dt} = \alpha_w \beta_g q_I + h_{r,w-g}(T_g - T_w) + h_{c,w-f}(T_f - T_w) + U_w(T_{am} - T_w). \quad (3)$$

It is noted that both the left and right sides of Eqs. (1)–(3) were divided by the same heat transfer area (cover or absorber area, $A_g = A_w$) to simplify the equations. Hence m_{f1} is the actual mass flow rate m_f divided by A_g or A_w .

To reduce the complexity during iterative calculation, an average temperature constant γ was pre-assumed:

$$T_f = \gamma T_{f,out} + (1 - \gamma) T_{f,in}, \quad (4)$$

where $\gamma=0.74$, a value recommended by Ong and Chow [38]. This value is higher than 0.5, due to the significant temperature difference for heat transfer and the thin boundary layer at the solar collector entrance area.

The calculations of heat exchange coefficients for radiation and convection within the solar collector channel can be found in most monographs concerning heat and mass transfer. They were proven to be long effective. The heat transfer coefficients for the channel cover are given as follows [39].

For radiation with absorber:

$$h_{r,w-g} = \frac{\sigma(T_w^2 + T_g^2)(T_w + T_g)}{\left(\frac{1}{\varepsilon_w} + \frac{1}{\varepsilon_g} - 1\right)}. \quad (5)$$

For convection with flowing air:

$$h_{c,f-g} = \frac{Nu_{f-g}\lambda_f}{D_s}, \quad (6)$$

$$Nu_{f-g} = 1.86 \left(\frac{Re_f Pr_f}{L_s/D_s}\right)^{1/3} \left(\frac{\mu_f}{\mu_g}\right)^{0.14} \quad (\text{for } Re_f < 2300), \quad (7)$$

$$Nu_{f-g} = 0.023 Re_f^{0.8} Pr_f^n \quad (\text{for } Re_f > 2300). \quad (8)$$

It is noted that D_s is an equivalent diameter, and it equals four times the channel cross-sectional area divided by the perimeter. The value of n is determined by the relative magnitude of the fluid and wall temperatures. When the wall heats the fluid, $n = 0.4$; when the wall cools the fluid, $n = 0.3$.

The air thermal conductivity λ_f is generally obtained by curve fitting formula, and an accurate one is [40]:

$$\lambda_f = 0.02442 + (10^{-4}(0.6992T_f)). \quad (9)$$

The other heat exchange coefficient for convection between the channel air and absorber, $h_{c,w-f}$, is also obtained by referring to Eqs. (6)–(9).

U_g is a coefficient used to calculate the total heat exchange between the cover and external environment. It also consists of two parts: convection with outdoor air ($h_{c,am-g}$) and radiation with sky ($h_{r,sky-g}$):

$$U_g = h_{c,am-g} + h_{r,sky-g}. \quad (10)$$

The convection part of U_g is given by [41]:

$$h_{c,am-g} = 5.7 + 3.8v_{am}. \quad (11)$$

The radiation part of U_g is given by [42]:

$$h_{r,sky-g} = \frac{\sigma\varepsilon_g(T_g^4 - T_{sky}^4)}{T_g - T_{am}}. \quad (12)$$

The sky temperature T_{sky} in Eq. (12) is associated with the outdoor air temperature T_{am} , and is calculated from an empirical formula [43]:

$$T_{sky} = 0.0552T_{am}^{1.5}. \quad (13)$$

The sky view factor of the absorber back side is zero. Hence, U_w , a coefficient used to calculate the total heat exchange between the absorber and external environment, consists of thermal conductivity in the insulation layer and convection with outdoor air:

$$U_w = \frac{1}{\frac{\delta_{ins}}{\lambda_{ins}} + \frac{1}{h_{c,am-ins}}}. \quad (14)$$

The calculation coefficient for the convection part, $h_{c,am-ins}$, is obtained by referring to Eq. (11).

2.2.2. EAHE pipe

Fig. 3 shows that the buried pipe is discretized along the horizontal direction. The assumptions made to simplify the simulation process were listed as follows.

- (1) The soil's physical properties are the same in all directions.
- (2) The temperature distribution within the pipe wall is uniform.
- (3) The soil is homogeneous and seamless.
- (4) It is an incompressible flow within the buried pipe.
- (5) The temperature distribution at the buried pipe section is uniform. Only the temperature change along the axial direction is considered.
- (6) Only sensible heat exchange is considered in the buried pipe.

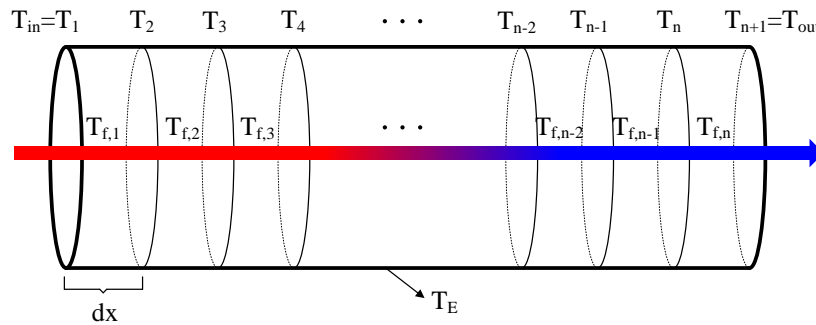


Fig. 3. Segmentation of EAHE pipe and flowing air within it

The governing equation for each element is:

$$m_f c_f dT_f = \pi D_E h_{c,E-f} (T_E - T_f) dx. \quad (15)$$

Eq. (15) is a first order linear differential equation, and its analytical solution is:

$$T_f(x) = T_E - (T_E - T_{in})e^{-\frac{\pi D_E h_{c,E-f} x}{c_f m_f}}. \quad (16)$$

The heat exchange coefficient, $h_{c,E-f}$, is obtained by referring to Eqs. (6)–(9). To increase the element temperature accuracy, Eq. (16) is applied to m discrete points within each element. Hence the element temperature $T_{f,i}$ is given by:

$$T_{f,i} = \frac{\sum_{j=1}^m \left[T_E - (T_E - T_i) e^{-\frac{\pi D_E h_{c,E-f} x_j}{c_f m_f}} \right]}{m}, \quad (17)$$

where x_j is a certain discrete point's coordinate.

Then the temperature change along the axial direction is obtained by substituting the discrete form of Eq. (15) with Eq. (17):

$$T_{i+1} = T_i - \frac{\pi D_E h_{c,E-f}}{c_f m_f} \left\{ \frac{\sum_{j=1}^m \left[T_E - (T_E - T_i) e^{-\frac{\pi D_E h_{c,E-f} x_j}{c_f m_f}} \right]}{m} - T_E \right\} dx. \quad (18)$$

2.2.3. Undisturbed soil temperature

The periodic variations in solar radiation and the ambient air temperature mainly influence the undisturbed soil temperature. Its excess temperature θ at depth z (m) and time τ (h) of a year can be obtained using the Fourier heat conduction differential equation as follows [44].

$$\frac{\partial \theta(z, \tau)}{\partial \tau} = a \frac{\partial^2 \theta(z, \tau)}{\partial z^2}. \quad (19)$$

$\theta(z, \tau)$ is equal to the difference between the soil temperature (at depth z and time τ) and the annual average ground surface temperature [44]:

$$\theta(z, \tau) = T_e(z, \tau) - \overline{T_{e,0}}. \quad (20)$$

The excess temperature at the ground surface exhibits a cosine pattern over a year as follows [44].

$$\theta(0, \tau) = \varphi \cdot \cos(\omega\tau), \quad (21)$$

where φ is the temperature fluctuation amplitude, and $\omega = \frac{2\pi}{8760h}$ is the frequency.

The undisturbed soil temperature field can be calculated by solving Eq. (19) with supplementary Eqs. (20) and (21) to yield:

$$T_e(z, \tau) = \overline{T_{e,0}} + \varphi \cdot e^{-z\sqrt{\frac{\omega}{2a}}} \cos\left(\omega\tau - z\sqrt{\frac{\omega}{2a}}\right). \quad (22)$$

2.2.4. Soil temperature rise

The subsoil heats or cools the fresh air when the outdoor temperature deviates from the thermal comfort limits. The soil temperature will gradually change if the annual average heating and cooling powers are out of balance. The assumptions made to simplify the simulation process were listed as follows.

- (1) The soil was regarded as a semi-infinite space with an adiabatic upper surface.
- (2) The buried pipe is a cylindrical heat source with infinite length.
- (3) The heat transfer between the soil and air is fast enough.

Green's function is typically used to show the temperature field caused by a point heat source [45]:

$$G(x, y, z, \tau; x', y', z') = \frac{1}{8[\sqrt{\pi a(\tau-\tau')}]^3} \exp\left[-\frac{(x-x')^2+(y-y')^2+(z-z')^2}{4a(\tau-\tau')}\right], \quad (23)$$

where (x', y', z') denotes the heat source's coordinate; τ' is the starting time.

The difference between the disturbed and undisturbed soil temperatures is defined as excess temperature (θ), and it can be obtained by integrating Eq. (23):

$$\theta = \frac{q_e}{\rho_e c_e} \int_0^\tau d\tau \int_{-\infty}^\infty \frac{1}{8[\sqrt{\pi a(\tau-\tau')}]^3} \exp\left[-\frac{(x-x')^2+(y-y')^2+(z-z')^2}{4a(\tau-\tau')}\right] dz. \quad (24)$$

$r = \sqrt{x^2 + y^2}$ is substituted to Eq. (24) to yield:

$$\theta(r, \tau) = \frac{q_e}{\rho_e c_e} \int_0^\tau \frac{1}{4a(\tau-\tau')} \exp\left[\frac{-r^2}{4a(\tau-\tau')}\right] d\tau. \quad (25)$$

The heat transfer process of a cylinder in an infinite space under constant heat flux is similar to that of a semi-infinite plane under constant heat flux. The analytical solution of the semi-infinite plane is relatively simple, which is convenient for engineering

calculations. Therefore, a fitting factor ($R_\theta = \frac{\theta_1}{\theta_2} = 1 + b \cdot Fo^n$) describing the ratio of the two excess temperature solutions in the two cases is introduced to further reduce the procedure complexity [46]. The excess temperature θ was simplified by the fitting results [46]:

$$\theta = \frac{q_e}{\pi \lambda_e (1 + 0.412 \cdot Fo^{0.426})} \sqrt{\frac{Fo}{\pi}}, \quad (26)$$

$$Fo = \frac{a\tau}{R_E^2}, \quad (27)$$

where Fo is dimensionless time. As we only focus on the soil temperature at the pipe wall surface, which affects the heat transfer efficiency. Hence r is substituted with the pipe radius R_E .

2.2.5. Buoyant pressure and resistances

The insulation layer performance of the chimney is ideal, and hence the chimney heat loss is not considered. The system buoyancy, ΔP_t , as the system driving force, is given by [48]:

$$\Delta P_t = \rho_0 g \Delta H \frac{(T_{s,out} - T_{E,in})}{T_0}, \quad (28)$$

where ρ_0 and T_0 are the reference density and temperature, respectively (take the outdoor parameters as the references).

The calculations for flow resistance losses can be found in most monographs concerning fluid mechanics. The frictional losses in the room are not considered. Hence the overall resistance loss includes three parts [49].

$$\Delta P_E = \left(\sum_i \xi_{i,E} + \xi_{f,E} \frac{L_E}{D_E} \right) \left(\frac{\rho_0 \cdot v_E^2}{2} \right) \text{ for buried pipe.} \quad (29)$$

$$\Delta P_S = \left(\sum_j \xi_{j,S} + \xi_{f,S} \frac{L_S}{D_S} \right) \left(\frac{\rho_0 \cdot v_S^2}{2} \right) \text{ for solar collector.} \quad (30)$$

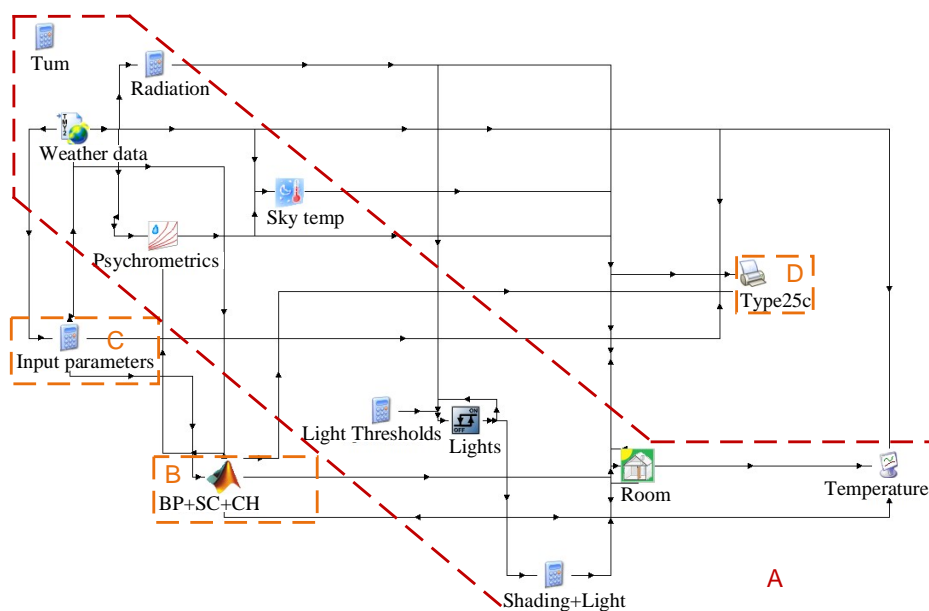
$$\Delta P_C = \left(\sum_k \xi_{k,C} + \xi_{f,C} \frac{H_C}{D_C} \right) \left(\frac{\rho_0 \cdot v_C^2}{2} \right) \text{ for chimney.} \quad (31)$$

2.3. Model solving

The procedure for coupling and solving the five sub-models was compiled with

MATLAB. A Building Project in TRNSYS simulated the room heat gain. The MATLAB and TRNSYS components were combined for joint implementation, and the conjunctive model is shown in Fig. 4.

We first launched a Building Project in TRNSYS. After setting the zone dimension, building location, and fraction of windows in external walls, the components in area A (see Fig. 4) were automatically generated. These components were used to calculate the room heat gain and room outlet air temperature. The thermophysical parameters of the room envelop are set by clicking the component named “Room” in area A. The mathematical descriptions for the room heat gain model refer to TRNSYS manual 5.4. The component named “BP+SC+CH”, which involves the sub-models of buried pipe, solar collector, vertical chimney, and soil temperature, is solved by MATLAB. The component named “Input parameters” is used to input the system geometric and soil’s thermophysical parameters. The component named “Type25c” is used to print and monitor critical operating parameters.



A: calculate the room heat gain and room outlet air temperature, generated by TRNSYS;
 B: solve the sub-models of buried pipe, solar collector, vertical chimney, and soil temperature by MATLAB;
 C: input the system geometric and soil thermophysical parameters;
 D: print and monitor key operating parameters;

Fig. 4. Components of TRNSYS–MATLAB simulation model

The parameter setting of this combined model is based on the authors’ previous work (see Ref. [35]). It is an experimental study concerning a full-scale SCEAHE system. The experimental test rig, dimensions of the system components, test method and devices, and test results are elaborated in detail in Ref. [35]. Important information used in this TRNSYS–MATLAB model is summarized in Tables 1 and 2. The TRNSYS–MATLAB model was also validated by the test results during the summer season from Ref. [35].

Table 1

Important information of coupled SCEAHE system

Items	Material	Geometry
Test chamber	Perforated brick	Internal dimensions 3 m (l) × 3 m (w) × 3 m (h)
Solar collector	Stainless steel and glass	7 m (l) × 1.5 m (w) × 0.3 m (h)
Vertical chimney	Stainless steel	6 m high with 0.3 m diameter
EAHE pipe	PVC	30 m long horizontal effective pipe with 0.3 m diameter

Table 2

Thermal properties of chamber envelop materials

Items	Density [kg/m ³]	Thickness [mm]	Thermal conductivity [W/(m·°C)]	Specific heat [kJ/(kg·°C)]	Heat storage coefficient [W/(m ² ·°C)]
Ceiling					
Polystyrene board	30	20	0.042	1.38	0.44
Reinforced concrete	2500	120	1.74	0.92	17.20
Cement mortar	1800	15	0.93	1.05	11.37
Wall					
Polystyrene board	30	20	0.042	1.38	0.44
Perforated brick	1400	200	0.58	1.05	7.92
Cement mortar	1800	15	0.93	1.05	11.37
Window					
Simple glass	2500	3	0.76	0.84	10.67

The hypothetical building for the simulation was located in a hot-summer/cold-winter zone (Chongqing, China). Zhou [48] conducted thermal response tests on ten boreholes located in ten representative districts of Chongqing, and Table 3 lists the results. The average value of 2.62 W/(m·K) for the ten thermal conductivity measurements was selected to be used in the present simulations.

Table 3

Results of thermal response tests in Chongqing.

Boreholes	Lithology	Depth of borehole [m]	Thermal conductivity [W/(m·K)]
1	Mudstone + sandstone	100	3.07
2	Mudstone + sandstone	100	2.87
3	Mudstone + sandstone	93	1.93
4	Mudstone + sandstone	78	2.1
5	Mudstone + sandstone	100	2.8

6	Mudstone + sandstone	88	2.55
7	Limestone + dolomite	83	2.56
8	Mudstone + sandstone	100	2.66
9	Limestone	100	2.57
10	Mudstone + sandstone	100	3.1

The calculation logic of the combined model is shown in Fig. 5. Which calculations are done by MATLAB and which are done by TRNSYS, are marked. The coupling strategy is elaborated as follows.

At time τ :

Step 1: A system airflow rate V_f is guessed to start the simulation. The temperatures of the system components and soil at buried pipe depth are known at time τ .

Step 2: The outlet air temperature $T_{E,out}$ and pressure loss ΔP_E of the buried pipe are calculated by Eqs. (18) and (29). The air mass flow rate m_f and air velocity v_E in the two equations are obtained from the guessed system airflow rate V_f and continuity equation.

Step 3: The calculated pipe outlet air temperature $T_{E,out}$ is used as the room inlet air temperature. The room heat gain and room outlet air temperature are calculated by TRNSYS components (area A in Fig. 4), in which the frictional loss is not considered.

Step 4: The calculated room outlet air temperature is used as the inlet air temperature $T_{s,in}$ for the solar collector. The outlet air temperature $T_{s,out}$ and pressure loss ΔP_s of the solar collector are calculated by Eqs. (4) and (30).

Step 5: The pressure loss of the vertical chimney ΔP_c is calculated by Eq. (31). As the vertical chimney is assumed to be well insulated, the system outlet air temperature equals the outlet air temperature of the solar collector $T_{s,out}$. The system buoyant pressure ΔP_t , as the total driving force, is calculated by Eq. (28) (system inlet and outlet air temperatures, $T_{E,in}$ and $T_{s,out}$, are used).

Step 6: The system is regarded as a quasi-steady-state at each moment during operation, and hence the total driving force ΔP_t should be equal to the total pressure loss ($\Delta P_E + \Delta P_s + \Delta P_c$). If the deviation is larger than our acceptable range, a new system airflow rate V_f is re-guessed and steps 1 to 5 are repeated. Bisection iterative method is used to adjust the guessed airflow rate V_f and equate the driving force and resistance. A convergence is eventually reached and the important parameters at this moment (airflow rate, indoor air temperature, pipe outlet air temperature, etc.) are outputted.

Move to time $\tau + \Delta\tau$:

The unsteady-state governing equations and supplementary equations—Eqs. (1) to (3), (5) to (14), and (26) to (27), are used to obtain the temperatures of the system components and soil at buried pipe depth at time $\tau + \Delta\tau$. Important parameters at time $\tau + \Delta\tau$ are also outputted by repeating steps 1 to 6. The time-varying system parameters are gradually calculated in this manner.

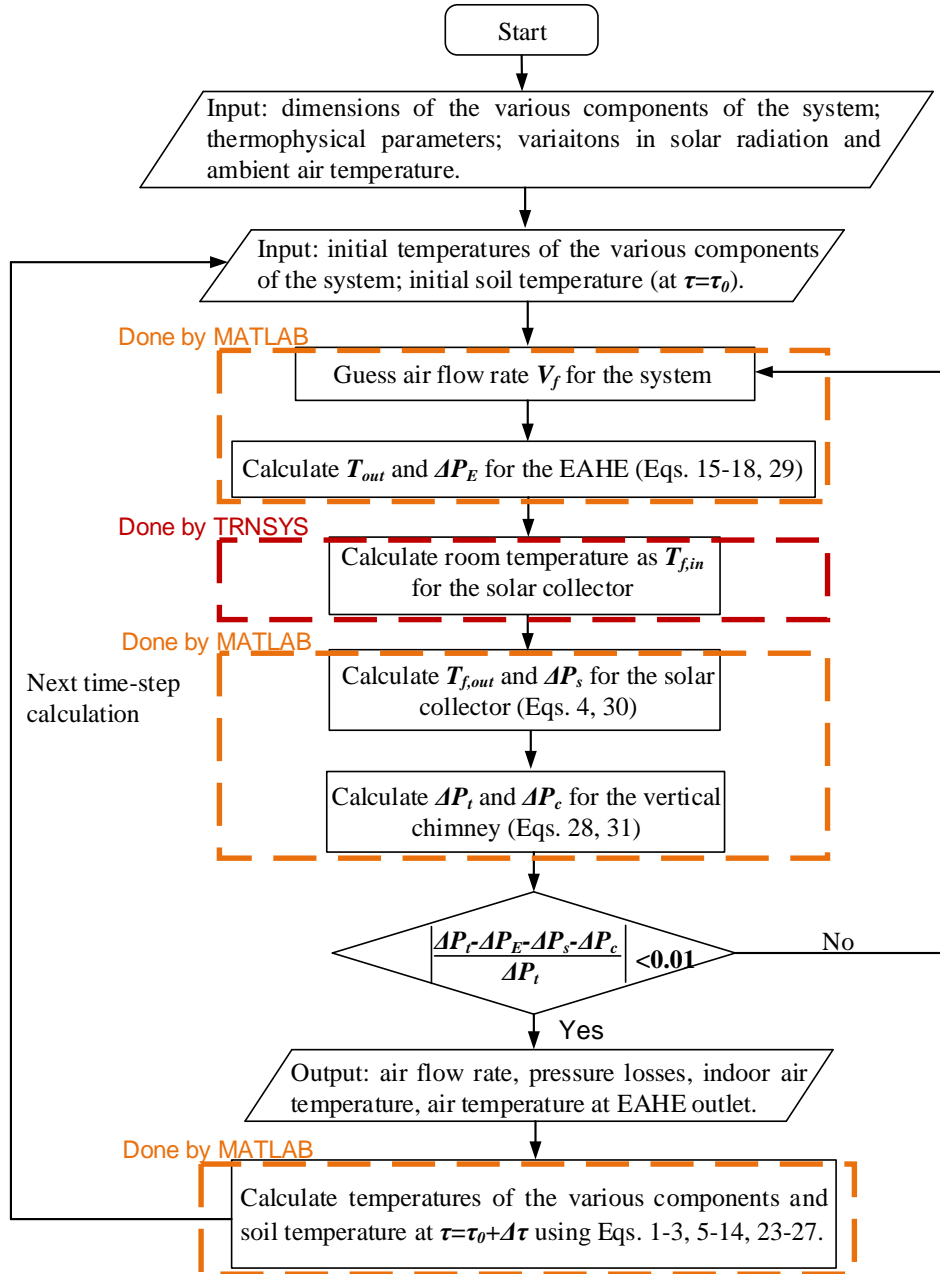


Fig. 5. Calculation logic of developed TRNSYS–MATLAB model

2.4. Validation

The validation was conducted by comparing the simulated results with the experimental data found in a published study. Ref. [36] detailedly elaborates the experimental test rig, dimensions of the system components, test method and devices, and test results of a full-scale SCEAHE system. It provides the basis to validate the proposed model in this study. Computations are implemented under the same initial conditions and boundaries as the experimental study. Three critical parameters—system airflow rate, supply air temperature, and indoor air temperature are chosen for the validation comparison.

Fig. 6 shows the measured and simulated system airflow rates. The variation tendencies of the two curves are similar. The airflow rate is approximately $60 \text{ m}^3/\text{h}$ owing to the low solar irradiance from 19:00 to 06:30. The heat released from the thermal mass maintains the buoyancy force and airflow rate during this stage with low solar irradiance. The two curves rise rapidly from 08:00. The simulated and measured airflow rates reach the peak values of 255.5 and $252.0 \text{ m}^3/\text{h}$, respectively. Furthermore, the airflow rates slightly reduce near 7:30 and 19:30 in both measurements and simulations, suggesting that the buoyancy force generated by the thermal mass or the SC is diminished. The mean error between the simulated and measured results is 14.0%. Fig. 7(a) compares the simulated and measured pipe outlet temperatures. The variation tendencies of the two curves are similar. Relatively steady outlet air temperature was recorded within a daily cycle, even during the daytime. During a daily cycle, the experimental and numerical outlet air temperature ranges are $26.5\text{--}27.4 \text{ }^\circ\text{C}$ and $25.3\text{--}27.7 \text{ }^\circ\text{C}$, respectively. In contrast, the ambient air temperature fluctuates with a large amplitude of $26.8\text{--}40.1 \text{ }^\circ\text{C}$. The mean error between the simulated and measured results is 5.5%.

The simulated and measured indoor air temperatures in a daily cycle are presented in Fig. 7(b). The variation tendencies of the two curves are similar. The experimental and numerical indoor air temperature ranges are $28.0\text{--}29.5 \text{ }^\circ\text{C}$ and $25.7\text{--}29.5 \text{ }^\circ\text{C}$, respectively. The mean error between the simulated and measured results is 6.4%.

Based on the above comparison, it can be concluded that the model herein can predict the performance of an SCEAHE system.

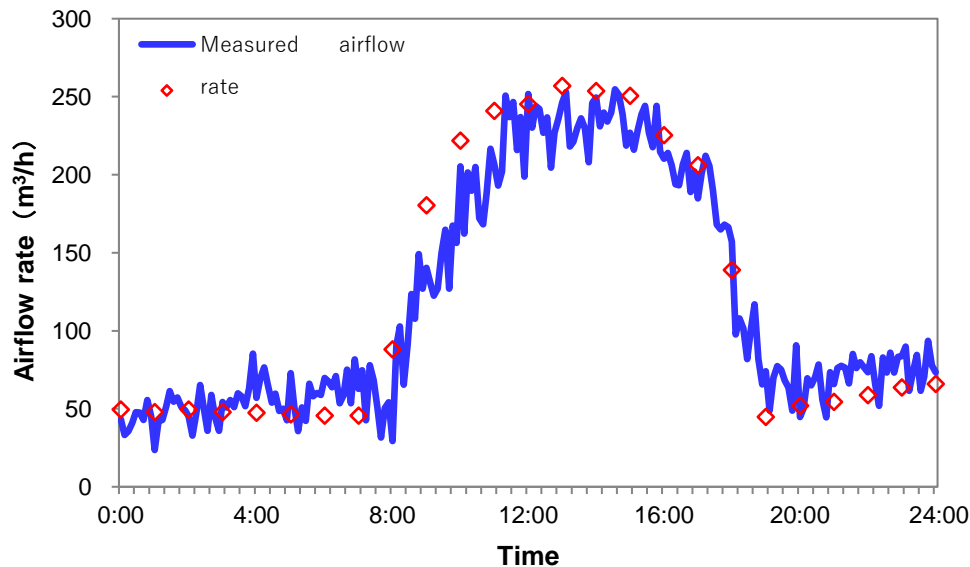


Fig. 6. Comparison of simulated and measured airflow rates

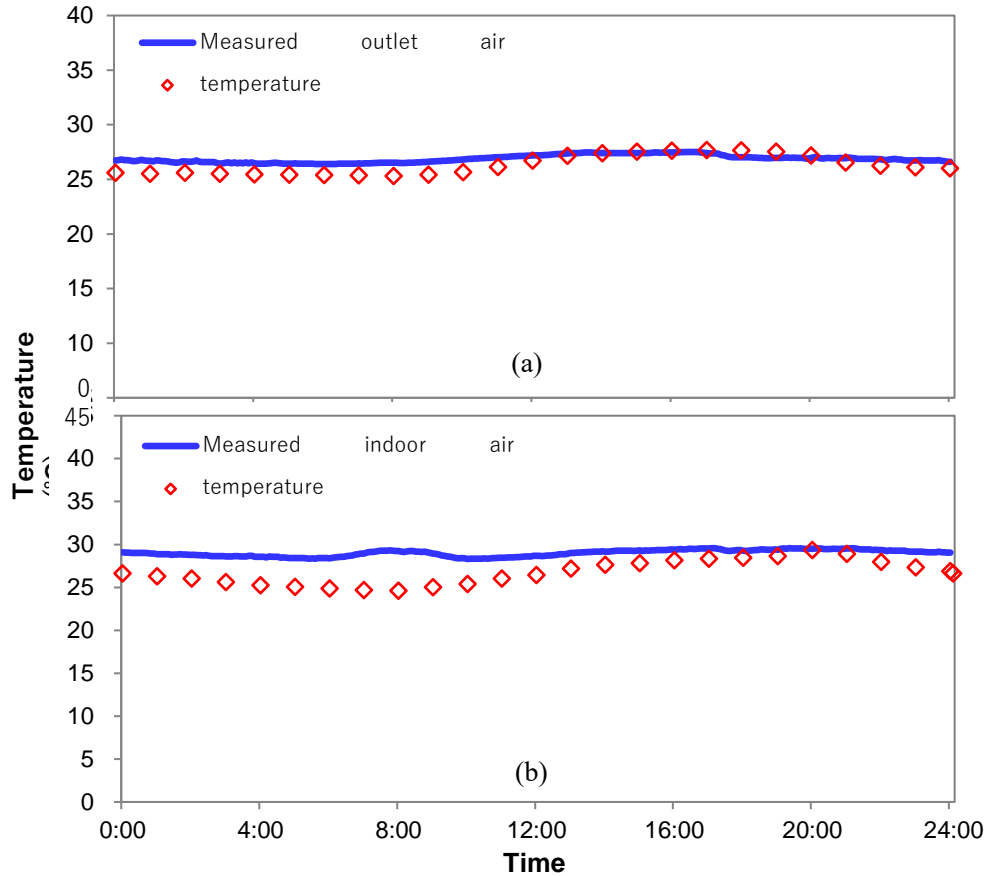


Fig. 7. Comparison of simulated and measured data: EAHE outlet air temperatures and indoor air temperatures

3. Results and discussion

3.1. Parametric study on main influencing parameters

The simulations for a parametric study were conducted under summer climates. The size and thermophysical parameters of the considered hypothetical building are listed in Tables 1 and 2. The hour-by-hour ambient temperature and solar irradiance, the same as those measured in the experimental tests in Ref. [36], are used as simulation boundaries. The ambient temperature and solar irradiance obtained from these experiments are presented in Fig. 8. It is noted that the solar irradiance is on horizontal plane. The initial temperature of each system component is assumed as the initial ambient temperature for the simulations. The initial soil temperature is set to 23.5 °C, which is consistent with the value from the field measurement.

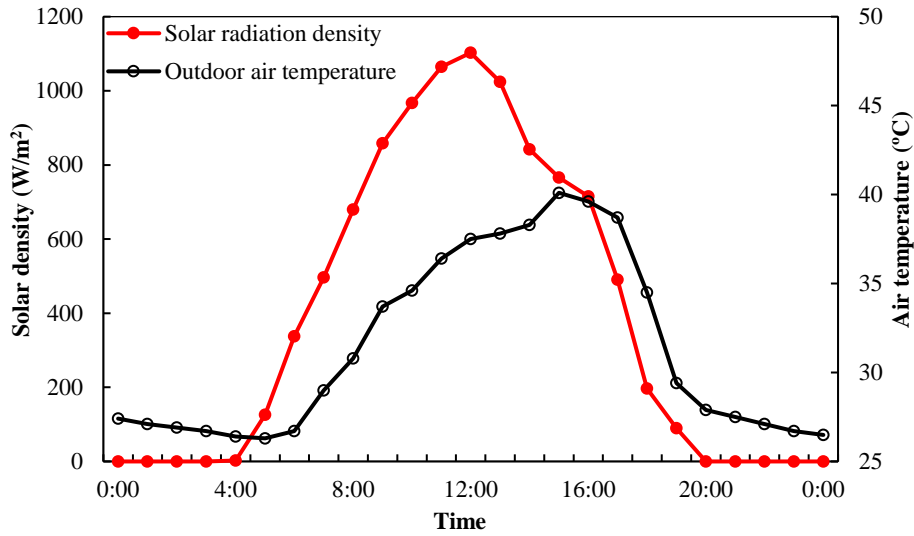


Fig. 8. Hourly solar radiation density and outdoor air temperature

3.1.1. Effects of pipe length

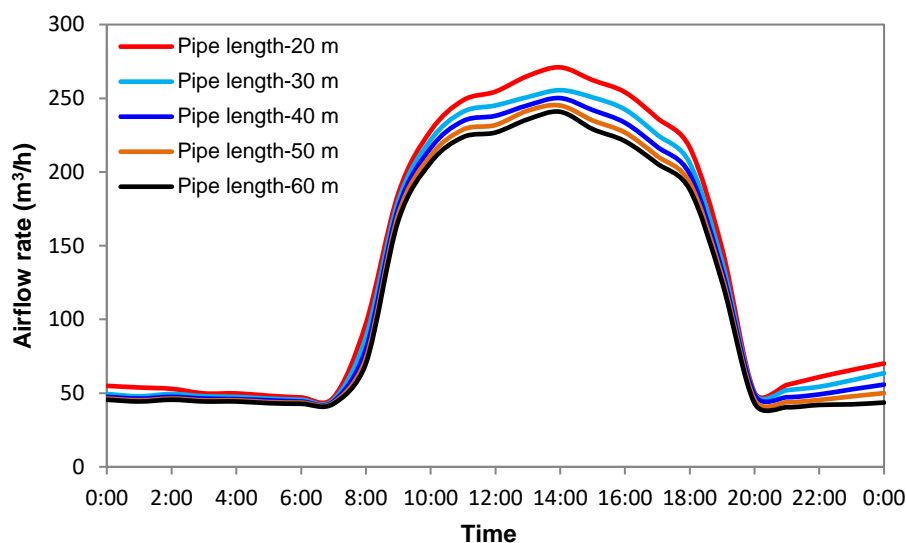
Though longer pipe length enlarges the heat transfer area, it increases the friction pressure loss along the pipe. Hence pipe length is an essential consideration for designing an SCEAHE system. During the simulation, the pipe length varies from 20 m to 60 m, whereas the other parameters are kept constant. Fig. 9(a) presents the variation in system air flow rate under a daily cycle with different pipe lengths. It is seen that a long pipe implies a low airflow rate during the daytime. The maximum system air flow rate descends from 270.0 to 237.0 m³/h as the pipe length increases from 20 m to 60 m. A long pipe leads to a low pipe outlet temperature (see Fig. 9(b)), which negatively affects the total buoyancy pressure. In contrast, the friction pressure loss increases as the pipe length increases. The above two factors jointly result in the reduced airflow rate.

Fig. 9(b) displays the effect of the pipe length on the air temperature at the EAHE pipe outlet. As shown, a long pipe implies a low pipe outlet temperature. Specifically, the maximum pipe outlet temperatures are 28.9 °C, 27.7 °C, 27.0 °C, 26.4 °C, and 26.1 °C for the pipe lengths of 20 m, 30 m, 40 m, 50 m, and 60 m, respectively. The fluctuation of the outlet air temperature is remarkably attenuated as the pipe length increases. For instance, the outlet air temperature varies within 25.3–28.9 °C for a pipe length of 20 m, whereas it fluctuates from 25.2 to 26.1 °C for a pipe length of 60 m. This is because the reduced airflow rate and the increased pipe length for heat exchange jointly reduce the air temperature at the EAHE outlet. However, it is noted that the decreasing rate of the outlet air temperature descends as the pipe length increases. It is caused by the decreasing temperature difference for heat exchange as the pipe length increases.

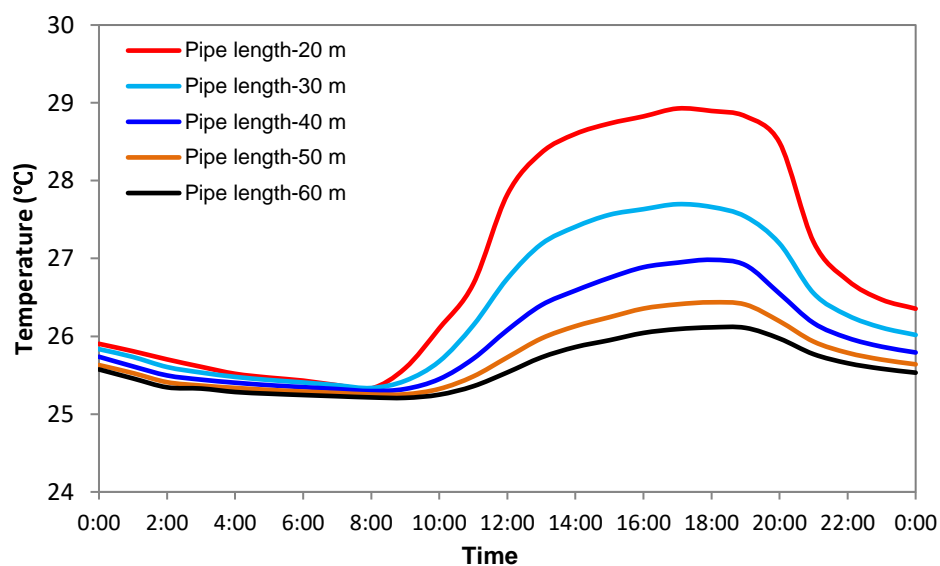
Fig. 9(c) presents the effect of the pipe length on the indoor air temperature. As seen, the indoor air temperature is low for a long pipe. The peak indoor air temperature drops from 30.5 °C to 28.2 °C when the pipe length increases from 20 m to 60 m. It means the reduction in pipe outlet temperature dominates the increment of cooling capacity

compared with the variation in air flow rate. A longer pipe leads to a higher cooling capacity. However, the increase in the cooling capacity will not be notable once the pipe length exceeds a specific value. Therefore, selecting an appropriate pipe length is critical in designing such an SCEAHE system.

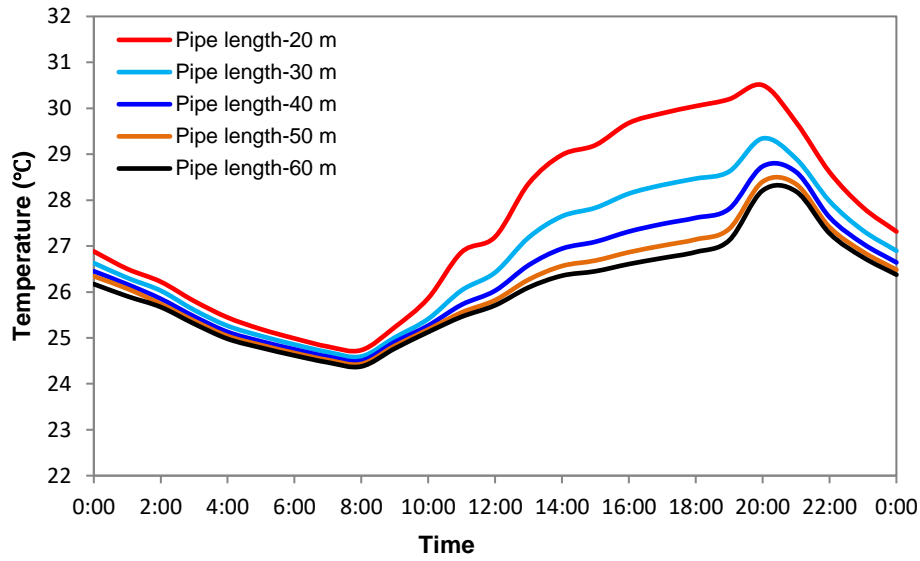
It is noted in Figs. 9(a) and 9(b) that the curves gradually become denser as the pipe length increases. This variation tendency is consistent with the results simulated by our previously proposed steady-state model (see Ref. [37]). In Ref. [37], the airflow rate and EAHE outlet air temperature decrease as the pipe length increases, with a descending decrease speed. Moreover, compared to the steady-state one, the dynamic simulation in this study shows more information—the daily variation tendency for each pipe length. For example, it is observed that the airflow rate fluctuated markedly from 50 to 250 m³/h within a daily cycle.



(a) Airflow rate



(b) EAHE outlet air temperature



(c) Indoor air temperature

Fig. 9. Effects of pipe length on (a) airflow rate, (b) EAHE outlet air temperature, and (c) indoor air temperature.

3.1.2. Effects of pipe diameter

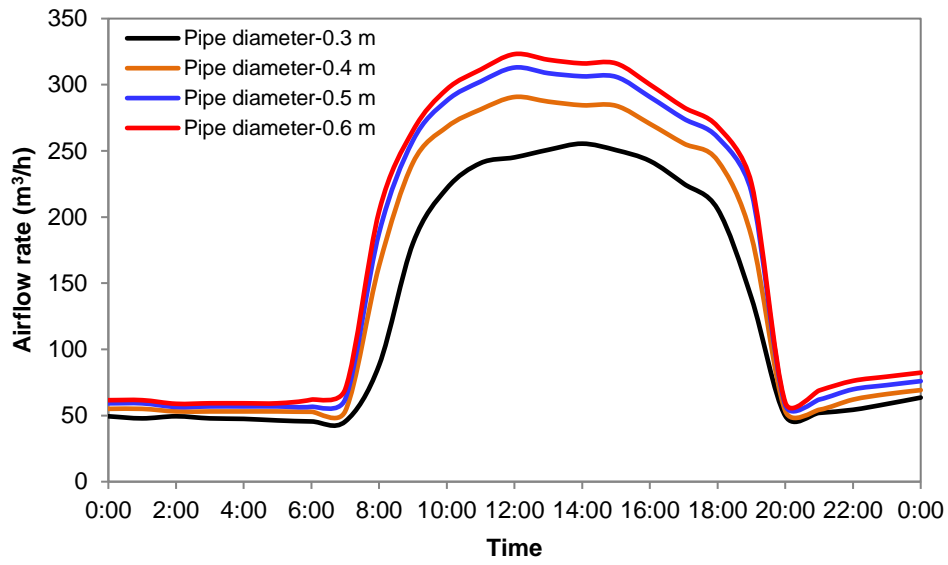
Fig. 10(a) presents the effect of the pipe diameter on the airflow rate. There is a positive correlation between the airflow rate and pipe diameter. The peak value changes from 255.5 to 323.2 m³/h as the pipe diameter varies from 0.3 to 0.6 m. This result can be attributed to the reduction in the pressure drop caused by the increasing pipe cross-sectional area.

Fig. 10(b) depicts the EAHE outlet air temperature variations for pipes with 0.3, 0.4, 0.5, and 0.6 m diameters. It is found that the pipe outlet temperature is significantly reduced compared to the ambient temperature, and a large pipe diameter implies a small reduction in the pipe outlet temperature. The maximum pipe outlet temperature is reduced from 29.7 to 27.7 °C as the pipe diameter changes from 0.3 to 0.6 m. It suggests that the increased heat exchange area is insufficient to compensate for the reduced heat exchange coefficient and increased air mass flow rate, which eventually increases the outlet air temperature.

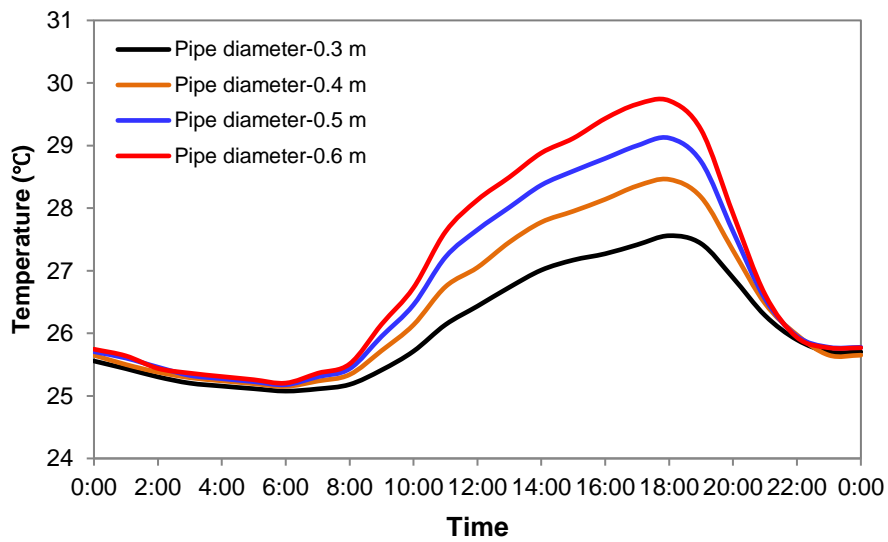
As shown in Fig. 10(c), the indoor air temperature rises with pipe diameter increases. The maximum indoor air temperatures are 29.5 and 31.0 °C for the pipe diameters of 0.3 and 0.6 m, respectively, growing by 1.5 °C. It suggests that the two factors affected by the pipe diameter, air flow rate and pipe outlet temperature, the latter plays a leading role in indoor air temperature. Consequently, increasing the pipe diameter cannot improve the indoor thermal environment.

In the steady-state results from Ref. [37], the airflow rate and EAHE outlet air temperature increase with the pipe diameter increases, with a descending increase speed. It is consistent with Figs. 10(a) and 10(b), in which the curves gradually become denser

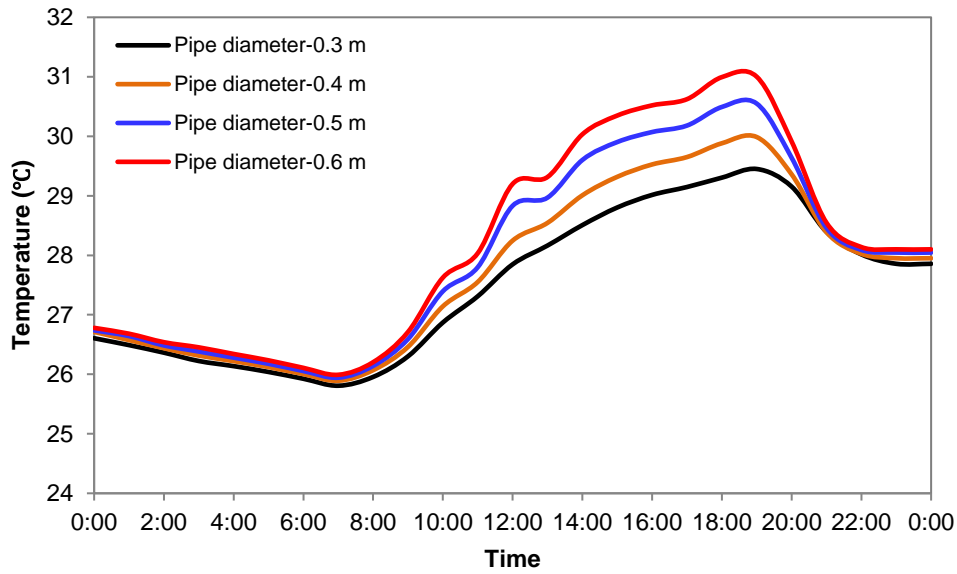
as the pipe diameter increases.



(a) Airflow rate



(b) EAHE outlet air temperature



(c) Indoor air temperature

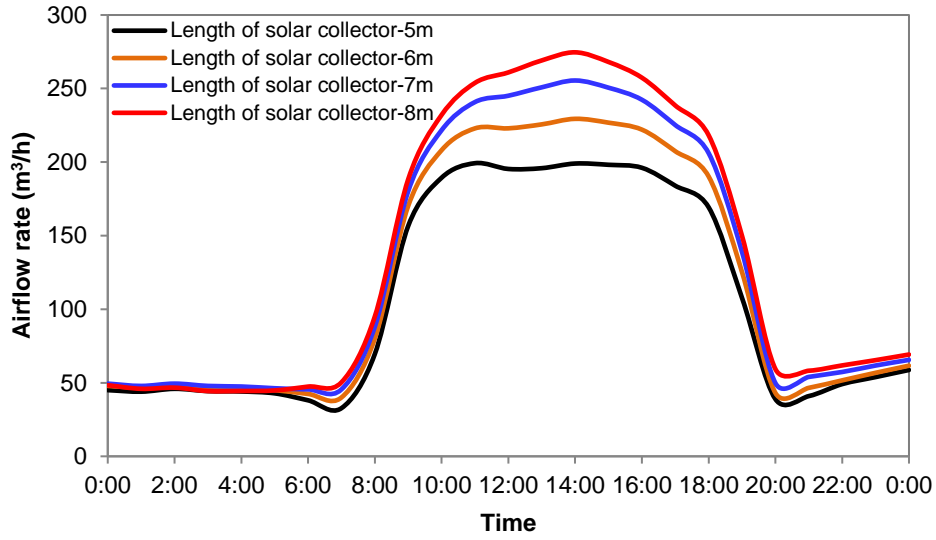
Fig. 10. Effects of pipe diameter on (a) airflow rate, (b) EAHE outlet air temperature, and (c) indoor air temperature

3.1.3. Effects of solar collector length

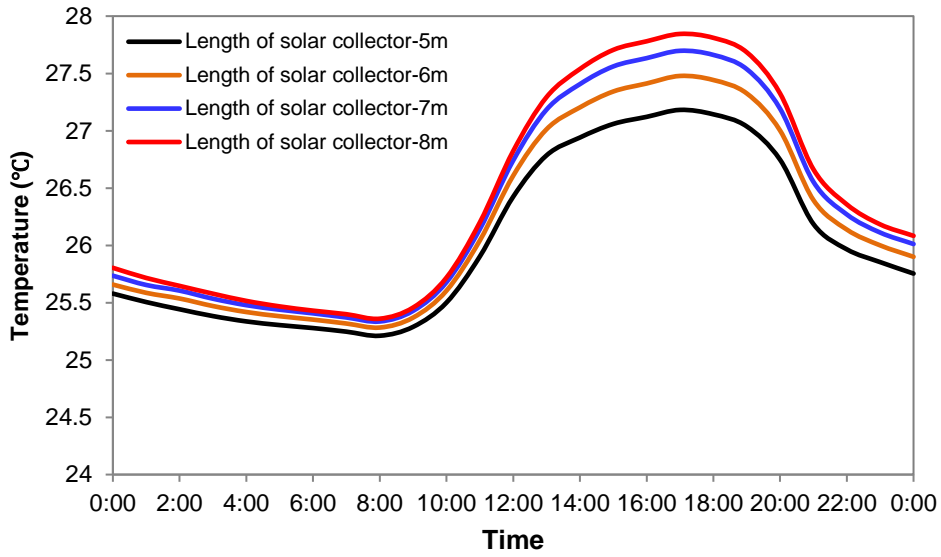
Figs. 11(a) and 11(b) show that both airflow rate and pipe outlet temperature increase as the solar collector length rises. This is because a longer solar collector is beneficial for increasing the solar heat gain and enhancing the buoyancy pressure difference. Specifically, the peak values of the air flow rate and outlet air temperature change from 199.1 to 274.6 m³/h and 27.2 to 27.8 °C, respectively, as the collector length varies from 5 to 8 m. The increment in the air flow rate shortens the heat transfer time per unit mass of air. Consequently, though the high air flow rate increases the heat exchange coefficient, the pipe supply air temperature is not reduced.

Fig. 11(c) shows that the indoor air temperature is slightly affected by the increase in the solar collector length. Though the maximum air flow rate is raised by 75.5 m³/h, the peak value of the EAHE outlet air temperature only increases by 0.6 °C when the collector length varies from 5 to 8 m. This suggests that the effect of the outlet air temperature on the indoor thermal environment is more remarkable than that of the airflow rate.

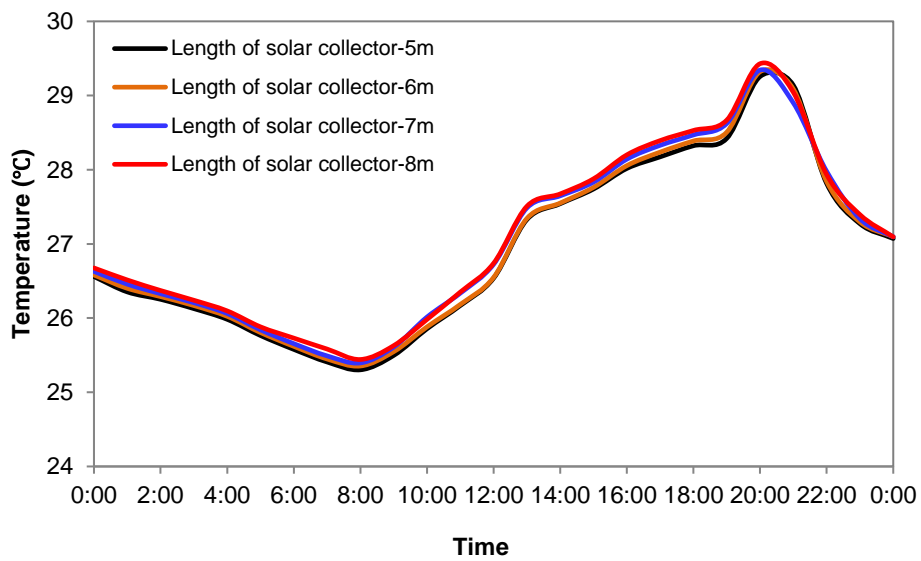
In Ref. [37], the simulated airflow rate and EAHE outlet air temperature under a steady state increase as the solar collector length increases. It is similar to the observed tendencies of the curves in Figs. 11(a) and 11(b).



(a) Airflow rate



(b) EAHE outlet air temperature



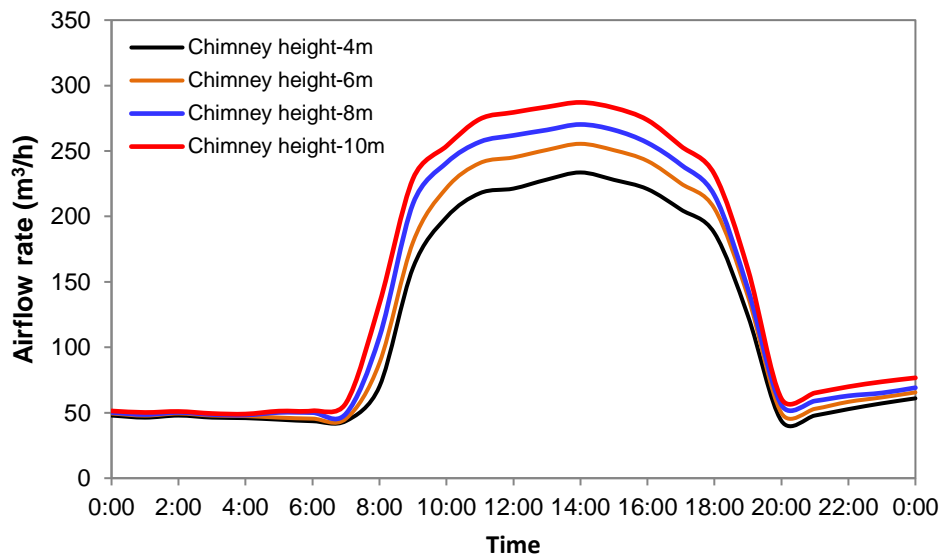
(c) Indoor air temperature

Fig. 11. Effects of length of solar collector on (a) airflow rate, (b) EAHE outlet air temperature, and (c) indoor air temperature

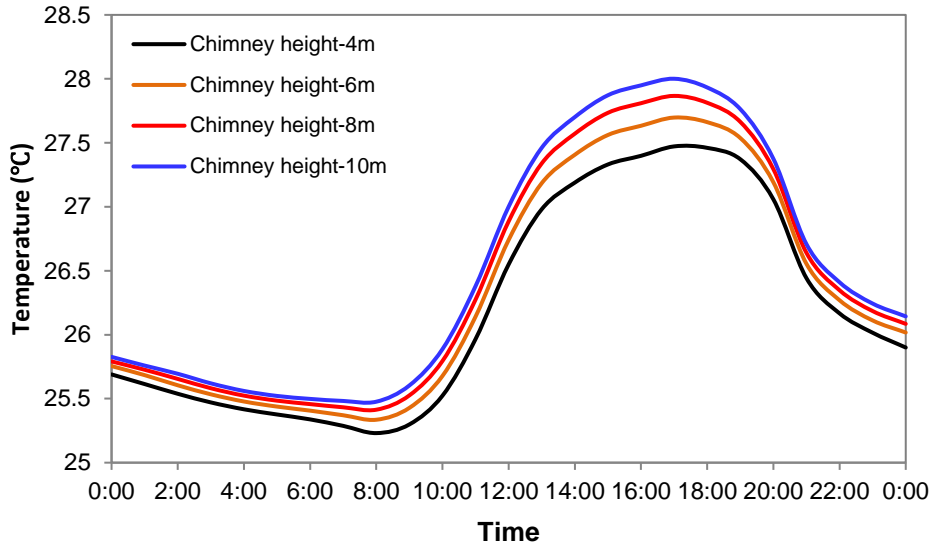
3.1.4. Effect of chimney height

The variations in the air flow rate and pipe outlet temperature are shown in Figs. 12(a) and 12(b). It is seen that the air flow rate and the pipe outlet temperature rise with the chimney length increases. The maximum air flow rate changes from 233.6 to 287.1 m^3/h , and the peak value of the outlet air temperature changes from 27.4 to 27.9 $^{\circ}\text{C}$, with the chimney length rises from 4 to 10 m. The air flow rate is changed by 53.5 m^3/h , whereas the pipe outlet temperature is changed by 0.5 $^{\circ}\text{C}$. The solar collector length has a more significant impact on both the air flow rate and outlet air temperature than the chimney height (compare Figs. 11 and 12). This finding is also consistent with the steady-state results from Ref. [37], in which the air flow rate and EAHE outlet air temperature also increase with the vertical chimney length increases.

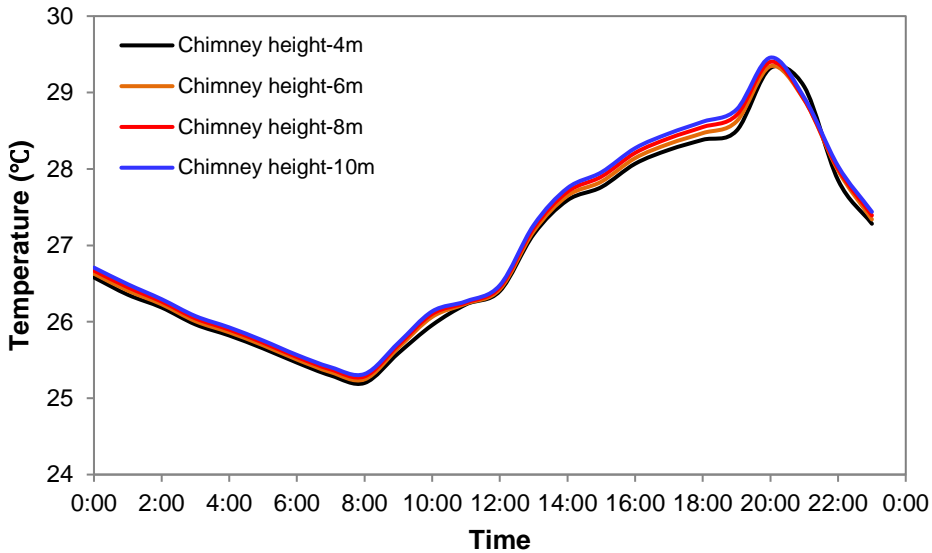
Fig. 12(c) shows that the chimney height also has a small impact on the indoor air temperature. The maximum indoor air temperature varies near 29.3 $^{\circ}\text{C}$ with the chimney height varies from 4 to 10 m. Therefore, an SCEAHE system with a high chimney could provide a high fresh air flow rate but not improve the indoor thermal environment.



(a) Airflow rate



(b) EAHE outlet air temperature



(c) Indoor air temperature

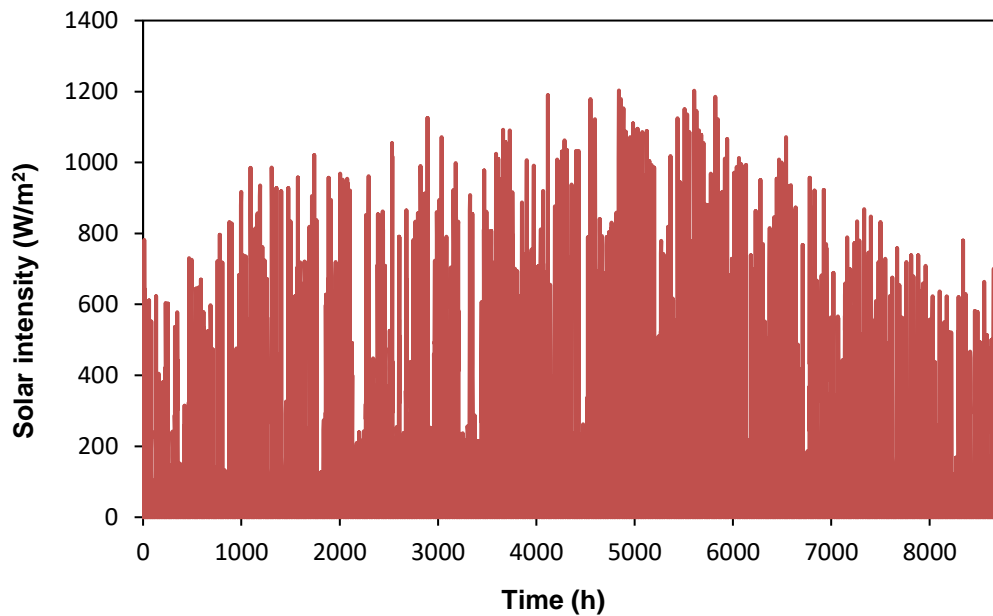
Fig. 12. Effects of chimney height on (a) airflow rate, (b) EAHE outlet air temperature, and (c) indoor air temperature

3.2. Annual performance of SCEAHE system

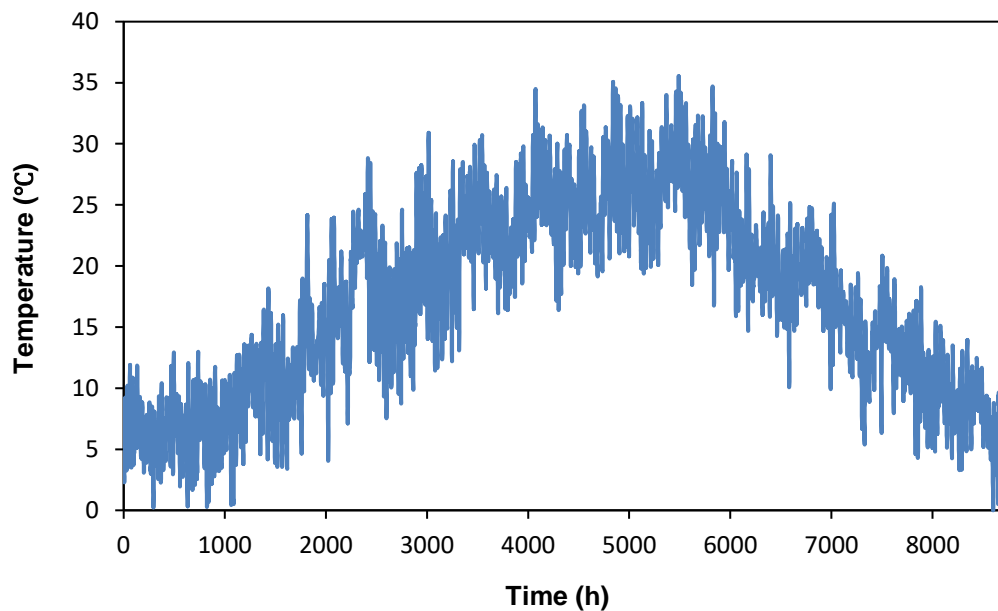
The annual performance simulations of the SCEAHE system were conducted considering it is operated in a pure passive mode. The simulation's initial values of the solar collector length, chimney height, EAHE pipe length, and pipe diameter were 6 m, 6 m, 50 m, and 0.3 m, respectively. The size and thermophysical parameters of the considered hypothetical building are listed in Tables 1 and 2.

Fig. 13 depicts the hourly solar radiation on horizontal plane and the outdoor air temperature distribution over a year obtained from the simulations. It is seen that the solar radiation is lower in the winter (December–February), spring (March–May), and

fall (October–November) seasons than that in summer (July–September). The peak solar intensity is as high as 1200 W/m^2 in summer. The outdoor air temperature has a similar variation tendency, and fluctuates within $0 \text{ }^\circ\text{C}$ – $35.5 \text{ }^\circ\text{C}$. This suggests that building heating and cooling needs exist in winter and summer, respectively.



(a) Hourly solar radiation



(b) Hourly outdoor air temperature

Fig. 13. Hourly solar radiation and outdoor air temperature distributions over entire year

3.2.1. Annual airflow rate

Fig. 14 shows the annual ventilation rate variation induced by the SCEAHE system. As shown, airflow rate fluctuations are due to the difference in buoyancy generated during daytime and night-time, and the fitting curve is concave. In summer, the daytime airflow rate varies near $260 \text{ m}^3/\text{h}$, and the nocturnal airflow rate varies close to $50 \text{ m}^3/\text{h}$. In contrast, in the other seasons, the daytime airflow rate increases to approximately $280 \text{ m}^3/\text{h}$, and the nocturnal airflow rate rises and exceeds $100 \text{ m}^3/\text{h}$. This suggests that the buoyancy generated by the SC has little change in the entire year. Although solar radiation is higher in summer than in other seasons, the higher outdoor air temperature in summer will also reduce the buoyant pressure [36]. However, in other three seasons, the buoyant pressure at night will be further enhanced by the lower ambient air temperature and assistance of the heating effect by the subsoil. This phenomenon will be further explained in Section 3.2.3.

It should be noted that though solar radiation is quite low ($100 \text{ W}/\text{m}^2$) sometimes, the SCEAHE system can provide an acceptable airflow rate during the daytime. It is concluded that this coupled passive SCEAHE system can operate appropriately even in the case of low solar intensity.

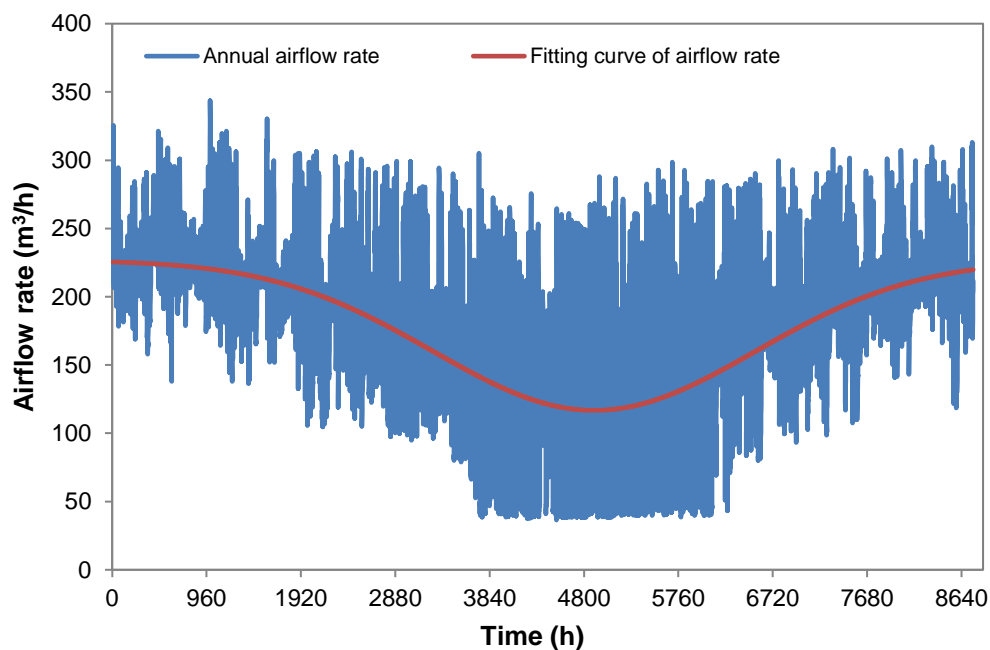


Fig. 14. Airflow rate induced by SCEAHE system over a whole year

3.2.2. Annual outlet air temperature of EAHE

The pipe outlet temperature, ambient temperature, and their difference are presented in Fig. 15. As shown, the daily and annual temperature variations at the EAHE outlet are strongly weakened compared to the outdoor air temperature. As the ambient temperature changes from 0 to $35.5 \text{ }^\circ\text{C}$, the EAHE outlet air temperature varies from

12.8 °C to 26.5 °C, with a yearly fluctuation range of 13.7 °C. The temperature reduction in ambient air by the buried pipe exhibits an opposite tendency to the ambient temperature. The EAHE is operated under a heating condition in winter, when the soil is warmer than the ambient air; the EAHE effectively elevates the fresh air temperature with a maximum increase of 16.0 °C. Once the ambient air temperature exceeds the soil temperature in summer, the excess heat is stored in the soil again; hence the EAHE is operated under a cooling condition. The fresh air temperature is reduced by as much as 11.0 °C. The heating and cooling capacities are beneficial to the indoor thermal environment. Furthermore, the EAHE pipe does not always cool the fresh air in summer; instead, it heats the fresh air at night as the ambient air temperature is low. The night ventilation can recover the cooling ability of the soil. Alternatively, when the ambient temperature is suitable, the EAHE pipe can be closed, and the cool outdoor air should be drawn into the indoor space through the opened window directly by the buoyancy force generated by the thermal mass of the building.

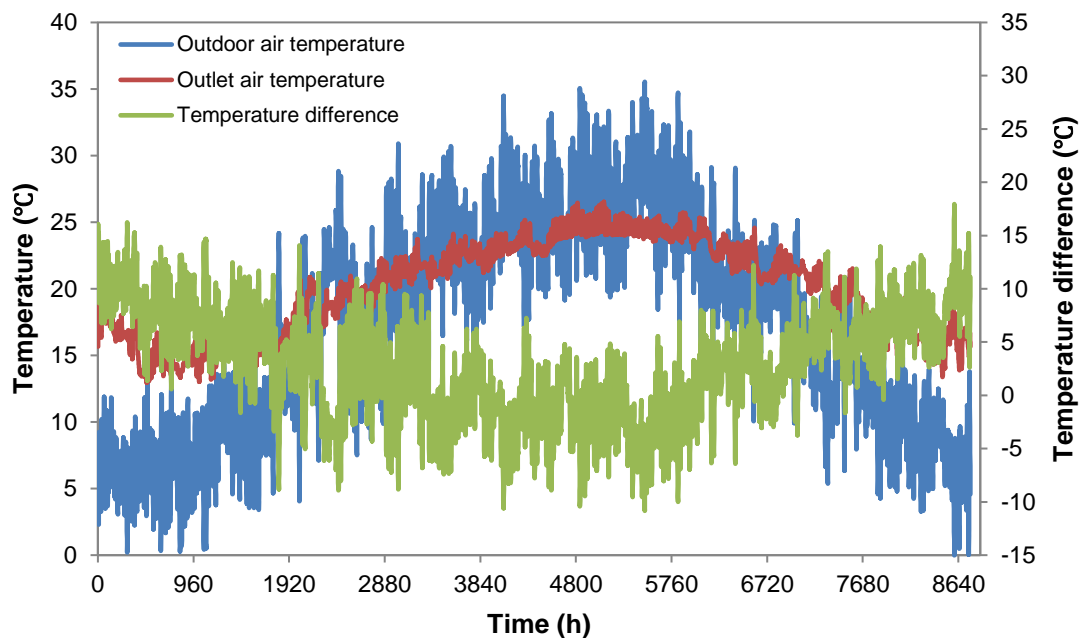


Fig. 15. EAHE outlet air temperature of SCEAHE system over entire year

3.2.3. Nocturnal ventilation driving force

It is known that the thermal mass is capable of generating buoyancy and air flow during the night-time on a summer day [51]. For an SCEAHE system, another heat source to generate the buoyancy force is the heating effect of the subsoil, when the ambient air temperature is lower than the soil temperature at night. As shown in Fig. 15, the ambient air temperature is significantly elevated by the subsoil, which increases the temperature difference between the indoor and outdoor air during night-time in winter and summer. Fig. 16 compares the annual room and ambient temperatures. The room temperature variation is also considerably attenuated. The yearly room air temperature fluctuates in

the range of 12.6–29.7 °C, whereas the ambient temperature fluctuates with a large amplitude of 26.8–40.1 °C. In winter, the indoor air temperature is remarkably higher than the outdoor air temperature owing to the heating effect of the EAHE. Hence, the heat released from the subsoil maintains the nocturnal buoyancy force and drives a higher air flow rate at winter nights. In summer, the indoor air temperature is lower than the outdoor air temperature during the daytime, whereas it is higher than the outdoor air temperature at night. Therefore, in summer, the nocturnal ventilation driving force can be generated by the coupling effect of the thermal mass and the subsoil. A small temperature difference between the indoor and outdoor air leads to a low nocturnal ventilation rate in summer.

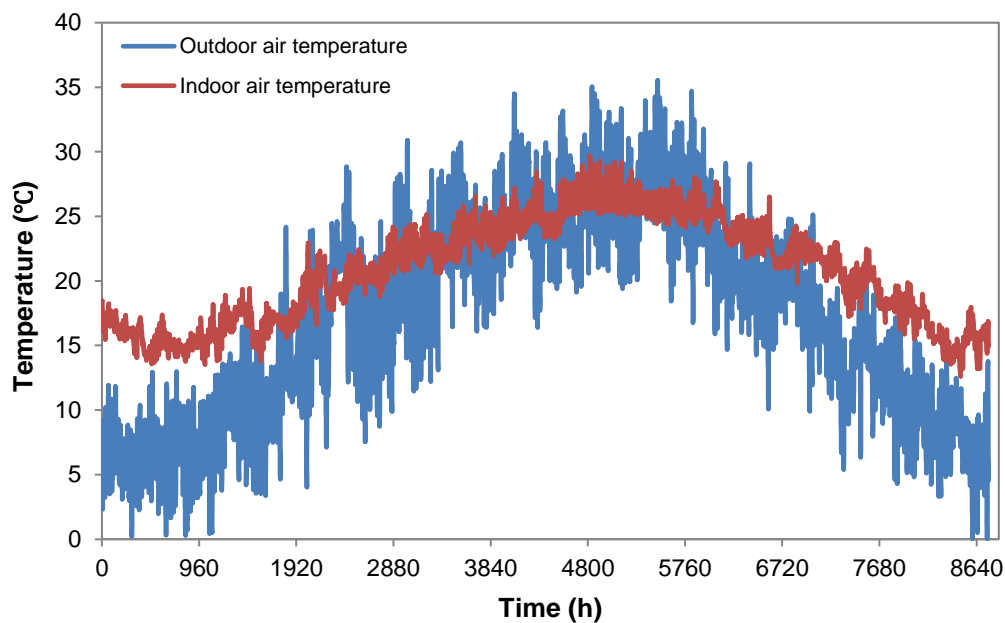


Fig. 16. Annual indoor and outdoor air temperatures.

3.2.4. Indoor thermal comfort

Fig. 17 shows the annual profiles of the indoor air temperatures with and without the SCEAHE system. The indoor air temperature for the case without the SCEAHE system is far beyond the thermal comfort temperature limits as recommended in the Chinese standard [52], both in summer and winter. Compared to the daily temperature fluctuation of the indoor air temperature in the case without the SCEAHE system, that in the case with the SCEAHE system is further reduced, and the yearly temperature fluctuation is also attenuated. The indoor air temperature profile falls within the thermal comfort temperature range for most time, particularly in summer. The average indoor air temperature can be reduced by 4.4 °C in summer, and the time of exceeding the upper thermal comfort limit of 28 °C is only 67 h. This suggests that the coupled system can appropriately regulate the indoor thermal environment without any other air-conditioning system in summer. Although the indoor air temperature is lower than 18 °C (lower thermal comfort limit) in most of the winter season, it is increased by an average

of 6.4 °C, with a maximum increase of 13.9 °C.

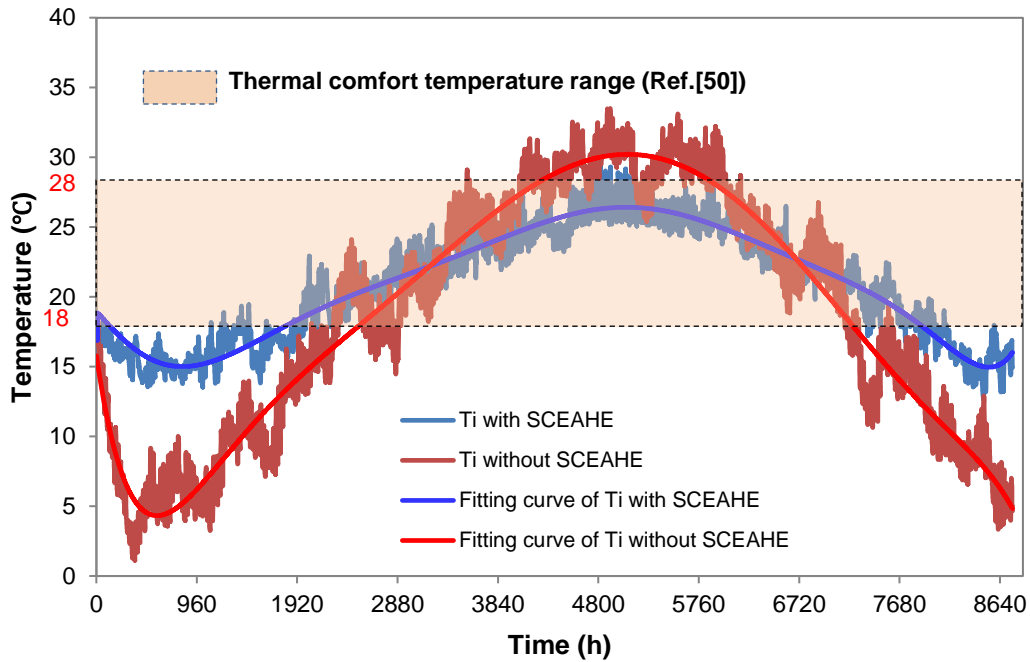


Fig. 17. Annual variations in indoor air temperatures with and without SCEAHE system

3.2.5. Variation in soil temperature

Fig. 18 shows the temperature variations of the soil surrounding the EAHE pipe and the undisturbed soil at 3-m depth during a one-year operation. It is observed that the soil surrounding the EAHE pipe is remarkably affected by the circulating ambient air. Although the soil temperature is disturbed by the ambient air, the overall variation in the soil temperature is similar to that in the undisturbed soil temperature, i.e. they present a cosine pattern. Initially, in the heating season months, the soil temperature decreases more rapidly than the undisturbed soil temperature, as the fresh air extracts heat from the soil; the lowest soil temperature occurs in March. In the cooling season months, the soil temperature increases, because the ambient air temperature rises and transfers heat to the soil; the highest soil temperature occurs in August. In addition, the temperature curve of the soil surrounding the EAHE is not as smooth as that of the undisturbed soil because of the effect of the ambient air. Contrastively, the original soil temperature is the lowest in May, whereas it is the highest in October. The annual temperature fluctuations of the soil surrounding the pipe and the undisturbed soil are 13.1°C–23.6 °C and 13.5 °C–21.1°C, respectively. The average temperatures of the soil surrounding the pipe and the original soil are 18.3 °C and 16.9 °C, respectively, i.e. the soil temperature is elevated by 1.4 °C after a one-year operation. This suggests that the SCEAHE system releases more heat to the ground during the cooling season than it absorbs from the ground during the heating season. Such a heat imbalance may increase the ground temperature over the years. Hence, optimizing the operating strategy, e.g.

by intermittent operation of the SCEAHE system, is vital for overcoming the problem of heat accumulation.

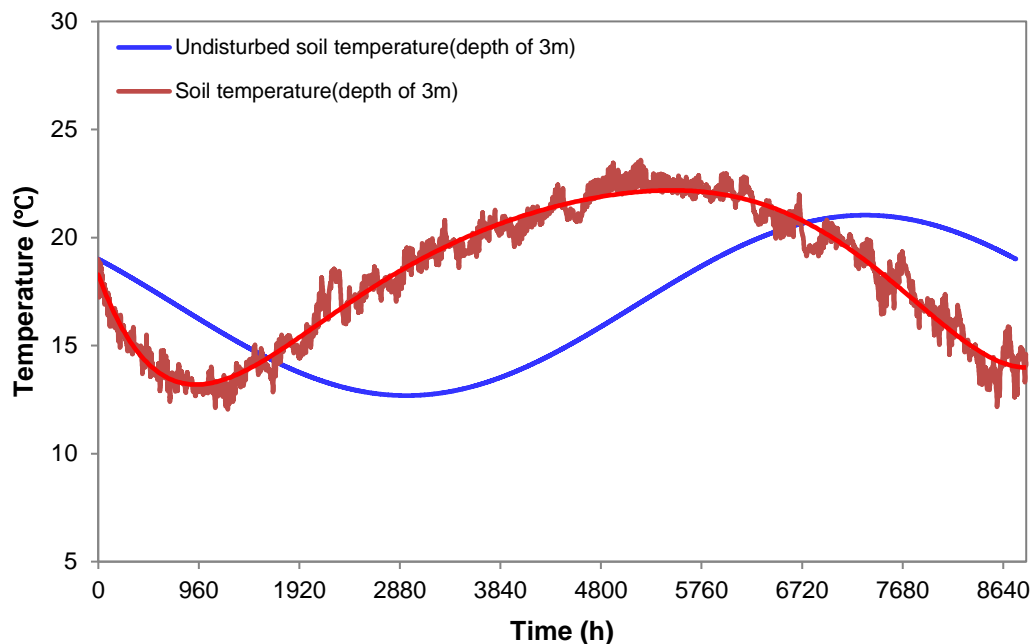


Fig. 18. Annual temperature variations of soil surrounding EAHE pipe and undisturbed soil at depth of 3 m

4. Conclusions and future work

This study establishes a dynamic model of a coupled solar chimney with an earth-to-air heat exchanger (SCEAHE) system to present its diurnal and annual performance. The system air flow rate, supply air temperature, and indoor air temperature are selected as the indicators to evaluate the system performance. The effects of the critical geometric parameters of the SCEAHE system on these three indicators are investigated in a diurnal period in summer. The main conclusions and future work are presented as follows.

4.1. Main conclusions

- (1) The pipe length and diameter are crucial for the diurnal SCEAHE system performance. A longer pipe or smaller diameter leads to a lower air flow rate, EAHE outlet temperature, and indoor air temperature, during summer climates. Nevertheless, the indoor thermal environment is not sensitive to the solar collector length and chimney height.
- (2) For a typical hot-summer/cold-winter region, the daytime buoyancy force is generated by the SC, whereas the nocturnal buoyancy force is induced by the thermal mass and/or the subsoil.
- (3) The yearly airflow rate varies in a concave pattern. In summer, the daytime airflow rate varies in the vicinity of 260 m³/h and the nocturnal airflow rate changes near 50

m³/h. In comparison, in the other seasons, the daytime airflow rate increases to approximately 280 m³/h, and the nocturnal airflow rate rises and exceeds 100 m³/h.

(4) The annual temperature fluctuation of the EAHE outlet air is reduced within 12.8 °C–26.5 °C by the thermal inertia of the subsoil. Moreover, the indoor air temperature profile falls within the thermal comfort temperature range for most time, particularly in summer. The average indoor air temperature can be reduced by 4.4 °C in summer and increased by 6.4 °C in winter.

(5) The average subsoil temperature is elevated by 1.4 °C after a one-year operation because more heat is released to the underground during the cooling season than the heat is absorbed from the underground during the heating season.

4.2. Future work

The diurnal and annual natural ventilation characteristics of an SCEAHE system have been studied by using a dynamic numerical model. The proposed model can be improved in these aspects: the buoyancy force can be calculated by the difference between the integral mean air temperature within the system and ambient air temperature instead of between the system inlet and outlet air temperatures; the latent heat transfer can be considered for the buried pipe.

The research focuses mainly on the effects of different parameters on the system performance and the temporal evolution of buoyancy force. It is easily found that the indoor thermal comfort requirement is not satisfied by applying a single SCEAHE system in an annual cycle. Therefore, to achieve the year-round indoor thermal comfort in a specific building under a given climatic condition, a new design method needs to be developed for determining the optimal SCEAHE system configuration concerning the system geometry and number. The findings would be beneficial for practical application of SCEAHE systems.

Acknowledgments

The authors acknowledge support from the National Natural Science Foundation of China (NSFC) under Grant No. 52078075 and 51708054, and 2018CDXYCH0015 supported by the Fundamental Research Funds for the Central Universities.

Reference

- [1] S. Ramkishore, R.L. Sawhney, I.J. Lazarus, V.V.N. Kishore, Recent advancements in earth air tunnel heat exchanger (EATHE) system for indoor thermal comfort application: A review, *Renewable and Sustainable Energy Reviews* 82 (2018) 2162–2185.
- [2] P.M. Cuce, S. Riffat, A state of the art review of evaporative cooling systems for building applications, *Renewable and Sustainable Energy Reviews* 54 (2016) 1240–1249.
- [3] M. Santamouris, D. Kolokotsa, Passive cooling dissipation techniques for buildings and other structures: The state of the art, *Energy and Buildings* 57 (2013) 74–94.
- [4] H.S. Bagiorgas, E. Chaideftou, M.N. Assimakopoulos, G. Mihalakakou, B.E. Psiloglou, E. Michalaina, The use of wind energy for passive cooling applications

- in western Greece, *Intelligent buildings international* (London) 1 (2009) 209–221.
- [5] M. Sameti, M.A. Jokar, Numerical modelling and optimization of the finite-length overhang for passive solar space heating, *Intelligent buildings international* (London) 9 (2017) 204–221.
- [6] A. Hadjadj, A. Atia, B.B. Haoua, M. Arıcı, N. Naili, A. Kaddour, Energy and exergy analyses of a helicoidal water to air geothermal heat exchanger for arid regions, *Energy Sources, Part A: Recovery, Utilization, and Environmental Effects* (2021) 1–16.
- [7] M. Dhahri, S. Nekoonam, A. Hana, M. Assad, M. Arıcı, M. Sharifpur, H. Sammouda, Thermal performance modeling of modified absorber wall of solar chimney-shaped channels system for building ventilation, *Journal of Thermal Analysis and Calorimetry* 145 (2021) 1137–1149.
- [8] N. Lebbihiat, A. Atia, M. Arıcı, N. Meneceur, Geothermal energy use in Algeria: A review on the current status compared to the worldwide, utilization opportunities and countermeasures, *Journal of Cleaner Production* 302 (2021) 126950.
- [9] Y. Li, S. Liu, J. Lu, Effects of various parameters of a PCM on thermal performance of a solar chimney, *Applied Thermal Engineering* 127 (2017) 1119–1131.
- [10] S. Liu, Y. Li, An experimental study on the thermal performance of a solar chimney without and with PCM, *Renewable Energy* 81 (2015) 338–346.
- [11] Y. Li, S. Liu, Experimental study on thermal performance of a solar chimney combined with PCM, *Applied Energy* 114 (2014) 172–178.
- [12] D.S. Lee, T.C. Hung, J.R. Lin, J. Zhao, Experimental investigations on solar chimney for optimal heat collection to be utilized in organic Rankine cycle, *Appl Energy* 154 (2015) 651–62.
- [13] A.A. Imran, J.M. Jalil, S.T. Ahmed, Induced flow for ventilation and cooling by a solar chimney, *Renew. Energy* 78 (2015) 236–244.
- [14] J.L. Xu, W.H. Liu, Study on solar chimney used for room natural ventilation in Nanjing. *Energy Build* 66 (2013) 467–9.
- [15] Z.D. Chen, P. Bandopadhyay, J. Halldorsson, C. Byrjalsen, P. Heiselberg, Y. Li, An experimental investigation of a solar chimney model with uniform wall heat flux. *Build Environ* 38 (2003) 893–906.
- [16] X.Q. Zhai, Y.J. Dai, R.Z. Wang, Experimental investigation on air heating and natural ventilation of a solar air collector, *Energy Build* 37 (2005) 373–81.
- [17] H.H. Al-Kayiem, K.V. Sreejaya, S.I.U. Gilani, Mathematical analysis of the influence of the chimney height and collector area on the performance of a roof top solar chimney, *Energy Build* 68 (2014) 305–11.
- [18] W. Du, Q.R. Yang, J.C. Zhang, A study of the ventilation performance of a series of connected solar chimneys integrated with building, *Renew Energy* 36 (2011) 265–71.
- [19] G.H. Gan, A parametric study of Trombe walls for passive cooling of buildings, *Energy Build* 27 (1998) 37–43.
- [20] O. Manca, S. Nardini, P. Romano, E. Mihailov, Numerical investigation of thermal and fluid dynamic behavior of solar chimney building systems, *J Chem Technol Metall* 49 (2014) 106–16.

- [21] N.K. Bansal, R. Mathur, M.S. Bhandari, Solar chimney for enhanced stack ventilation, *Build. Environ.* 28 (1993) 373–377.
- [22] C. Afonso, A. Oliveira, Solar chimneys: simulation and experiment, *Energy and Buildings* 32(1) (2000) 71–79.
- [23] Z. Liu, Z.J. Yu, T. Yang, S. Li, M. El Mankibi, L. Roccamena, et al., Experimental investigation of a vertical earth-to-air heat exchanger system, *Energy Conversion and Management* 183 (2019) 241–251.
- [24] Z. Liu, P. Sun, M. Xie, Y. Zhou, Y. He, G. Zhang, et al., Multivariate optimization and sensitivity analysis of an experimental vertical earth-to-air heat exchanger system integrating phase change material with Taguchi method, *Renewable Energy* 173 (2021) 401–414.
- [25] EREC Reference Briefs, Earth Cooling Tubes, U.S. Department of Energy (2002).
- [26] G. Gan, Simulation of dynamic interactions of the earth–air heat exchanger with soil and atmosphere for preheating of ventilation air, *Applied Energy* 158 (2015) 118–132.
- [27] S. Ahmed, M. Amanullah, M. Khan, M. Rasul, N. Hassan, Parametric study on thermal performance of horizontal earth pipe cooling system in summer, *Energy Convers Manag* 114 (2016) 324–37.
- [28] V. Kabashnikov, L. Danilevskii, V. Nekrasov, I. Vityaz, Analytical and numerical investigation of the characteristics of a soil heat exchanger for ventilation systems, *Int J Heat Mass Transf* 45 (2002) 2407–18.
- [29] M. Bojic, G. Papadakis, S. Kyritsis, Energy from a two-pipe, earth-to-air heat exchanger, *Energy* 24 (1999) 519–523.
- [30] J. Khedari, B. Boonsri, J. Hirunlabh, Ventilation impact of a solar chimney on indoor temperature fluctuation and air change in a school building, *Energy and Buildings* 32 (2000) 89–93.
- [31] Z. Liu, Z.J. Yu, T. Yang, M. El Mankibi, L. Roccamena, Y. Sun, et al., Experimental and numerical study of a vertical earth-to-air heat exchanger system integrated with annular phase change material. *Energy Conversion and Management* 186 (2019) 433–449.
- [32] M. Maerefat, A.P. Haghighi, Passive cooling of buildings by using integrated earth to air heat exchanger and solar chimney, *Renewable Energy* 35 (2010) 2316–2324.
- [33] H. Li, Y. Yu, F. Niu, M. Shafik, B. Chen, Performance of a coupled cooling system with earth-to-air heat exchanger and solar chimney, *Renew. Energy* 62 (2014) 468–477.
- [34] Y. Yu, H. Li, F. Niu, D. Yu, Investigation of a coupled geothermal cooling system with earth tube and solar chimney, *Appl. Energy* 114 (2014) 209–217.
- [35] Y. Li, T. Long, X. Bai, L. Wang, W. Li, S. Liu, J. Lu, Y. Cheng, K. Ye, S. Huang, An experimental investigation on the passive ventilation and cooling performance of an integrated solar chimney and earth-air heat exchanger, *Renewable Energy* 175 (2021) 486–500.
- [36] T. Long, D. Zheng, W. Li, Y. Li, J. Lu, L. Xie, S. Huang, Numerical investigation of the working mechanisms of solar chimney coupled with earth-to-air heat exchanger (SCEAHE), *Solar Energy* 230 (2021) 109–121.

- [37] T. Long, N. Zhao, W. Li, S. Wei, Y. Li, J. Lu, et al., Natural ventilation performance of solar chimney with and without earth-air heat exchanger during transition seasons. *Energy* 250 (2022) 123818.
- [38] K.S. Ong, C.C. Chow, Performance of solar chimney, *Solar Energy* 7 (2003) 41–17.
- [39] T.L. Bergman, A.S. Lavine, F.P. Incropera, D.P. DeWitt, *Fundamentals of heat and mass transfer*, Wiley Press (2011).
- [40] E.W. Lemmon, R.T. Jacobsen, Viscosity and thermal conductivity equations for nitrogen, oxygen, argon, and air, *Int J Thermophys* 25(1) (2004) 21–69.
- [41] W.H. McAdams, *Heat Transmission*. 3rd Ed, New York: McGraw-Hill (1994).
- [42] K.S. Ong, A mathematical model of a solar chimney, *Renew Energ* 28 (2003) 1047–1060.
- [43] W.C. Swinbank, Long-wave radiation from clear skies, *Q. J. R. Meteor. Soc* 89 (1964) 339.
- [44] ASHRAE handbook–HVAC systems and equipment, Atlanta, Georgia: American Society of Heating, Refrigerating and Air-Conditioning Engineers, Inc. ch. 11 (2002).
- [45] H.S. Garslaw, J.C. Jeager, *Conduction of heat in solids*, Oxford: Oxford Press (1959).
- [46] X. Liu, D. Wang, Z. Fang, Cylindrical heat transfer model and simplified calculation of ground source heat pump with vertical buried pipe, *Journal of Shandong Institute of Architecture and Engineering* 16(1) (2001) 47–51 (in Chinese).
- [47] P.M. Gerhart, R.J. Gross, J.I. Hochstein, *Fundamentals of Fluid Mechanics*, Addison-Wesley Pub. Co. (1992).
- [48] S. Zhou, Thermal physical properties of typical stratum and operational characteristics of ground source heat pump system in Chongqing area, Doctor's degree thesis (2016) (in Chinese).
- [49] J. Zhou, G. Zhang, Y. Lin, Y. Li, Coupling of thermal mass and natural ventilation in buildings, *Energy and Buildings* 40(6) (2008) 979–986.
- [50] MOHURD, Code for Design of Heating Ventilation and Air Conditioning (GB 50019-2003), Beijing (2003) (in Chinese).